DISPERSION LAW FOR VIRTUALLY IMAGED PHASED ARRAY (VIPA) SPECTRAL DISPERSERS

A Thesis

Submitted to the faculty

of

Purdue University

by

Alberto Vega

In Partial Fulfillment of the

Requirements for the Degree

of

Master of Science in Electrical and Computer Engineering

December 2002

This thesis is dedicated to all those who believed that I could accomplish this.

ACKNOWLEDGEMENTS

I would like to thank Dr. Weiner for his support and advice, Avanex and TecOptics for providing devices, and Dan Leaird for his support in the lab.

TABLE OF CONTENTS

LIST OF FIGURES

ABSTRACT

Vega, Alberto M.S.E.C.E., Purdue University, December 2002. Dispersion Law for Virtually Imaged Phased Array (VIPA) Spectral Dispersers. Major Professor: Andrew M. Weiner.

With growing demands in communications, optical systems and their components are used to push lightwave communication to greater speeds. One of important components in these systems is a spectral disperser. This device spatially separates different frequencies and can be used backwards to combine frequencies. This has specific use in combining or separating unique lightwave channels into and out of a single fiber. This is known as wavelength division multiplexing. Also, a spectral disperser can be used for pulse shaping by separating different frequencies for specific amplitude or phase modulation. This can be used to generate trains of short pulses and for the correction of dispersion of ultra-short pulses in fiber optics.

Typical devices known for spectral dispersion are the prism and diffraction grating, where both devices can take white light and spread out the colors of the spectrum spatially. Another recently introduced device, resembling a Fabry-Perot etalon and called the virtually imaged phased array (VIPA), performs the same function as the other two devices. The VIPA has been experimentally tested and has been shown to have certain advantages over the other devices, but a complete understanding of its functionality has not been formed until now. This thesis presents for a first time a quantitative derivation of a dispersion law that characterizes the operation of the VIPA. The presented law is experimentally tested through the usage of three different VIPAs. In the end, the derived law shows remarkable agreement with captured data and shows its accuracy for different VIPA constructions.

1. INTRODUCTION

A prism is a basic device that performs spatial dispersion of visible wavelengths. A beam of white light is shone into a prism and the output is a rainbow of colors. This occurs because different wavelengths of light travel at different speeds, or have different indices of refraction, in certain media. There is also a diffraction grating that performs the same task of spatial dispersion, but its method of operation is through a periodic pattern on the face of the grating, unlike the material dependent method of the prism. A third device, the topic of this thesis, is an etalon with certain modifications that takes advantage of multiple reflections of a light source and the interference between these reflections to provide dispersion.

Motivation behind using a modified etalon instead of using one of the other mentioned devices is polarization insensitivity, ease of construction, low cost, and greater dispersive capabilities. [1]

This modified etalon or Virtually Imaged Phased Array (VIPA), the name will be explained later, has many applications and has demonstrated a potential or current use in fiber communications. The VIPA has demonstrated capabilities for usage in Wavelength Division Multiplexing (WDM) communications [2]. Data streams with different optical center wavelength are combined into one fiber for transmission across one data channel and separation at the receiving point. Figure 1.1 shows a simple diagram of a WDM communication system. The VIPA can serve as a de-multiplexer or multiplexer by spatially separating the bands around the different center wavelengths for detection at the receiving end or by spatially combining the different frequencies by operating the VIPA in backwards fashion at the transmission end.

The VIPA also has a commercial application in dispersion compensation, where very short pulses of light in fiber optics are broadened in time because different wavelengths travel at different speeds in the fiber [3]. The VIPA can spatially separate these different frequencies and direct them toward a contoured mirror with spatial delays that correct for the delays in fiber. See figure 1.2 for an example of a dispersion compensation setup. Dispersion is compensated by giving the wavelengths that travel

faster in the fiber a longer spatial delay on the contoured mirror and the slower traveling wavelengths a shorter spatial delay.

Pulse shaping is another application where the VIPA can be used. Dispersion compensation is a form of pulse shaping, but a fixed contoured mirror is used given that the characteristics of the fiber do not change over time. With pulse shaping, a liquid crystal modulator in front of a flat mirror, see figure 1.3, could be used to modify the amplitude and phase of the different frequencies in place of a fixed mirror [4]. This could be used to create pulse trains that represent a string of data bits.

Although the VIPA has been shown useful in many applications and has demonstrated its functionality experimentally, an understanding of the functionality of this device has been missing. A law describing the phase matching conditions, and other characteristics, of the VIPA is presented here. This law is similar to the dispersion law for the diffraction grating. This thesis will first cover background information about the Fabry-Perot interferometer, a very similar device to the VIPA. Next, the physical device differences between the Fabry-Perot etalon and VIPA will be shown. The theory and derivation of the VIPA dispersion law and equation for the free spectral range (FSR) follow the device differences. After the theory is presented, experimental verification shows the remarkable accuracy of the derived equations. Within the experimentation, three different devices are used, and each process is described.

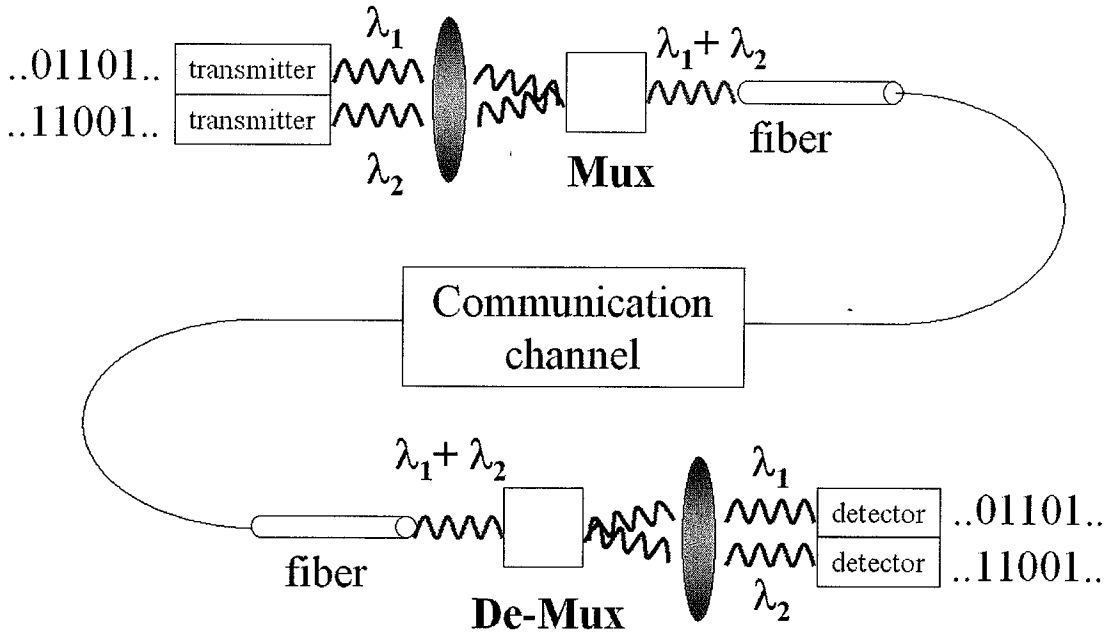

Fig. 1.1. Simple example of a WDM communication system

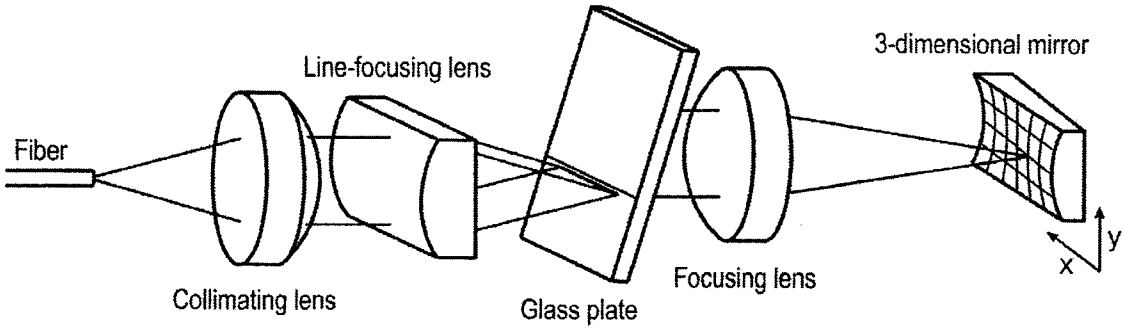

Fig. 1.2. Example of a dispersion compensation setup using a VIPA (glass plate) [3].

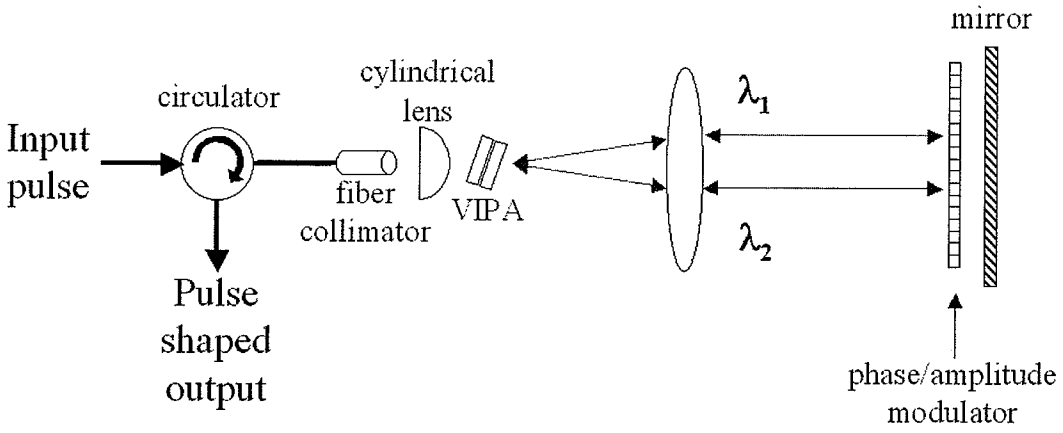

Fig. 1.3. Diagram of pulse shaping setup using a VIPA.

2. THE FABRY-PEROT INTERFEROMETER

The Fabry-Perot interferometer is a device consisting of two parallel boundaries that have certain reflectivities which creates a cavity. The cavity can be created by applying a reflective coating on both sides of a flat piece of glass as in figure 2.1, which creates a solid etalon [7]. An air spaced etalon can be created by placing a spacer between two pieces of glass which have the inside surface coated with reflective material [7], which is shown in figure 2.2.

The interferometer functions when a plane wave is input into the etalon either parallel to the normal of the input surface or at an oblique angle. For this case, we will consider the case where the input is parallel to the normal of an air spaced cavity. The plane wave reaches the first boundary with phase exp(-j*k*0). The amount of the energy that is transmitted continues on to the second interface and arrives with phase exp(-j*k*d) in figure 2.3, where d is the thickness of the cavity and k is the propagation constant within the cavity. The energy that is between the interfaces undergoes a series of reflections and interferes with previous reflections. As the energy bounces back and forth, resonant frequencies constructively interfere and non-resonant frequencies destructively. The survival of certain frequencies is determined by the spacing of the two interfaces or cavity thickness. For resonant waves, the round trip distance (two times the cavity thickness) is an integer number of wavelengths. In terms of phase, the phase acquired from the round trip distance must be an integer multiple of 2π. An equation which describes the transmission of the interferometer as a function of wavelength is

$$T(\omega) = \left\{ \frac{(1-R_1)(1-R_2)}{(1-\sqrt{R_1R_2})^2 + 4\sqrt{R_1R_2}\sin^2(\omega nd/c)} \right\} \tag{2.1}$$

where R_1 and R_2 are the reflectivities with respect to power of the first and second surfaces respectively, n is the index of the material in the cavity, d is the thickness of the cavity, and c is the speed of light in vacuum [5]. The above equation describes the

transmission of the etalon, and is concerned with the ratio of the power of the light coming out of the etalon to that of the light incident upon the etalon. In order to derive it, we take a look at the electric field just beyond the first reflective surface heading toward the second surface. This field will be called E_{tot}^{+} and consists of the original input plane wave and reflections of it.

$$E_{tot}^{+} = \sum_{n=0}^{\infty} E_n^{+} = E_0^{+} + E_1^{+} + E_2^{+} + \ldots \tag{2.2}$$

is the expression for the total field traveling toward the second surface. The equation is the sum of the incident wave just after the first boundary E_0^{+}, the reflection off the second surface and the first surface E_1^{+}, the second reflection E_2^{+}, and so on. Figure 2.4 shows a diagram of these reflected waves. Looking at an observation plane just behind the first reflective surface, E_0^{+} is equal to E_0 since we choose that point to be where in the input wave has zero phase, where E_0 is equal to the amplitude of the original incident wave times the transmission coefficient. E_1^{+} is equal to $E_0*\Gamma_1\Gamma_2*\exp(-jk2d)$ due to the phase accumulated from one round trip, where Γ_1 and Γ_2 are the complex reflection coefficients for the electric field. E_2^{+} is given by $E_0*(\Gamma_1\Gamma_2)^2*[\exp(-jk2d)]^2$ because this wave has seen both reflective surfaces twice and has accumulated twice the amount of round trip phase. The field for the rest of the reflections is quite similar and follows suit of the previous expressions. The summation of the above terms can be expressed by

$$E_{tot}^{+} = E_0\left(\frac{1}{1-\Gamma_1\Gamma_2 e^{-j2kd}}\right) \tag{2.3}$$

and the intensity of E_{tot}^{+} can be written as

$$I^{+} = \frac{E_0^2}{2\eta}\frac{1}{1-2\left|\Gamma_1\Gamma_2\right|\left[1-2\sin^2(2kd)\right]+\left|\Gamma_1\Gamma_2\right|^2} \tag{2.4}$$

where η is the intrinsic impedance of air (or other material). If the reflection coefficients are assumed to be real, the above equation can be rewritten as

$$I^{+} = \frac{E_0^2}{2\eta}\left[\frac{1}{\left(1-\sqrt{R_1R_2}\right)^2 + 4\sqrt{R_1R_2}\sin^2(2kd)}\right] \quad (2.5)$$

Since we are interested in the transmitted intensity, I_{TRANS}, we see that it is equal to the intensity at the observation plane times the transmissivity of the second reflective surface [$I_{TRANS}=I^{+}\cdot T_2= I^{+}\cdot(1-R_2)$]. Also, the intensity of the first forward moving wave is equal to $E_0^2/2\eta$ which is also equal to $I_{INC}\cdot T_1$, the intensity incident on the etalon times the transmissivity of the first reflective surface. Combining equation 2.5 with the relations mentioned above, we now obtain

$$T(k) = \frac{I_{TRANS}}{I_{INC}} = \left[\frac{(1-R_1)(1-R_2)}{\left(1-\sqrt{R_1R_2}\right)^2 + 4\sqrt{R_1R_2}\sin^2(kd)}\right] \quad (2.6)$$

where k can be replaced with ωnd/c to reproduce equation 1. This derivation took large steps in the interest of presenting a brief path to producing the transmission of an etalon with a zero degree input angle. For a more thorough derivation, please see the proper references.

This device serves as an optical filter. A detector on the opposite side of the input would see that certain constructive wavelengths have much higher intensity than the non-resonant wavelengths. Figure 2.5 shows an example of the transmission of the etalon for varying frequencies. There are a few terms that assist in describing the characteristics of the interferometer. The frequency spacing between the peaks is called the free spectral range. The quality factor of the cavity or selectivity of the resonance is given by the ratio of the center frequency to the full width of the spectral peaks at half maximum. Quality factor is represented by

$$Q = \frac{\nu_0}{\Delta\nu_{FWHM}} \quad (2.7)$$

where ν_0 is the center frequency of the peak and $\Delta\nu_{FWHM}$ is the width in terms of frequency of the peak at half maximum [5]. Cavity finesse, another way of measuring the filtering capabilities, is given by the ratio of the free spectral range to the full width at half max of the spectral peaks [5].

$$F = \frac{c/2nd}{\Delta\nu_{FWHM}} \quad (2.8)$$

Here, $\Delta\nu_{FWHM}$ is the width of the intensity peak in terms of frequency at half maximum.

An interferometer with high quality factor and finesse is desired to resolve narrow spectral channels for information or observation. The FSR is adjusted for specific applications and is given by

$$FSR = \frac{c}{2nd\cos\theta} \quad (2.9)$$

where θ is the input angle into the etalon [9]. When the input angle is zero, or perpendicular to the surface of the etalon, the FSR is c/2nd, which is used to determine the FSR of a laser cavity.

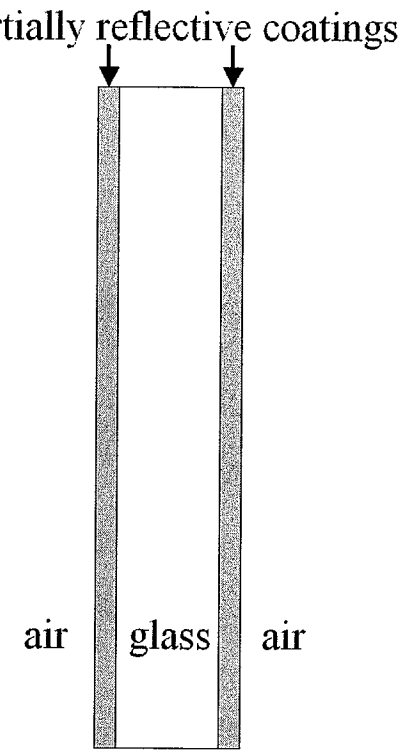

Fig. 2.1. Solid etalon.

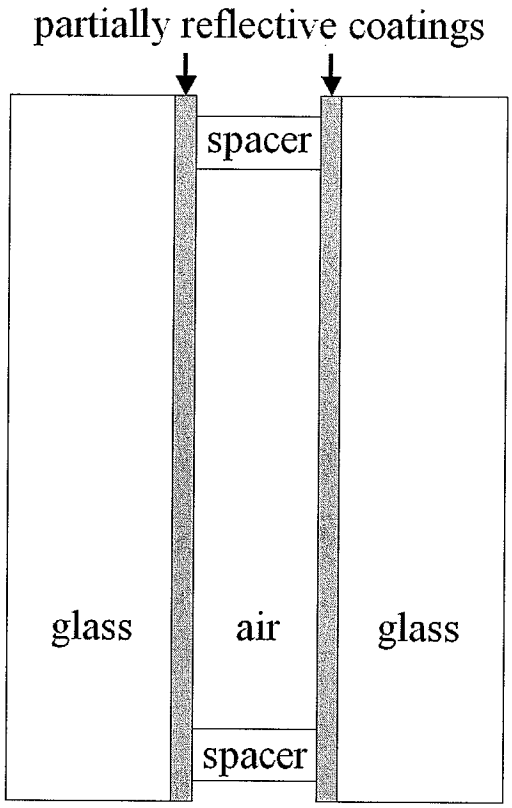

Fig. 2.2. Air spaced etalon.

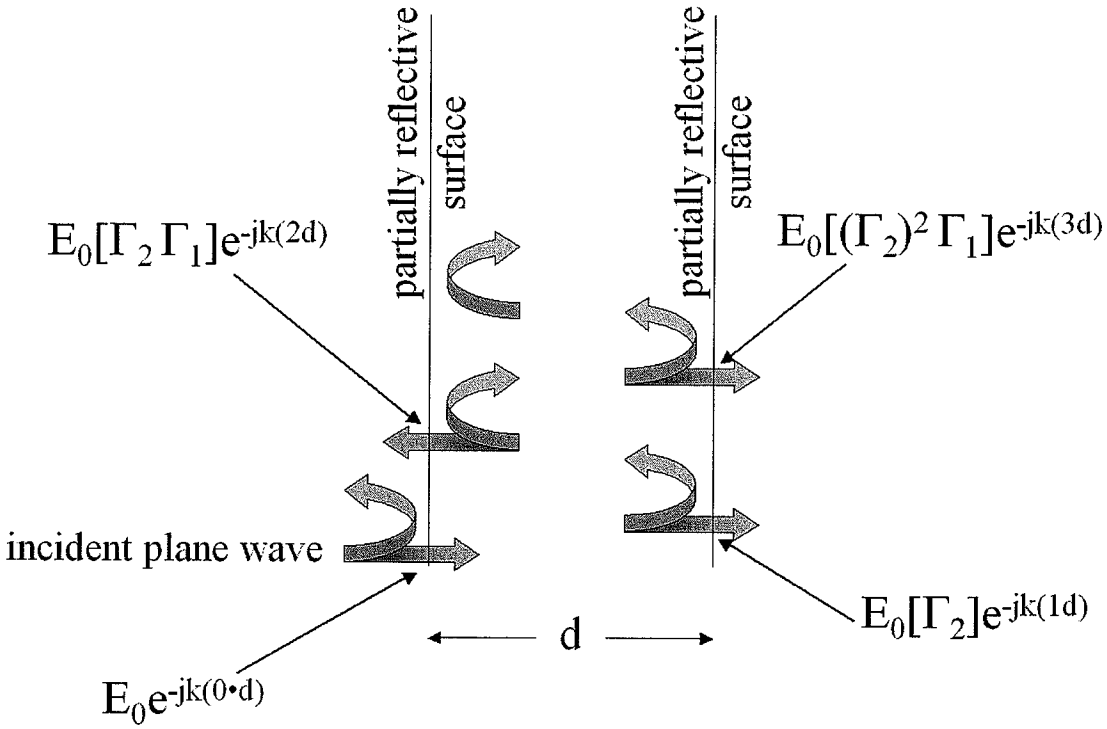

Fig. 2.3. Plane waves in cavity.

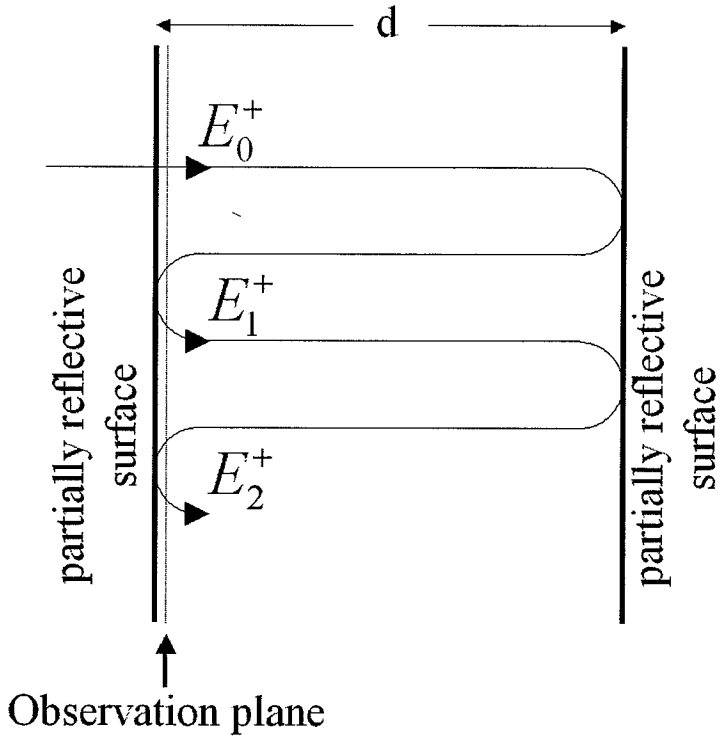

Fig. 2.4. A view of the forward traveling waves in the Fabry-Perot Interferometer

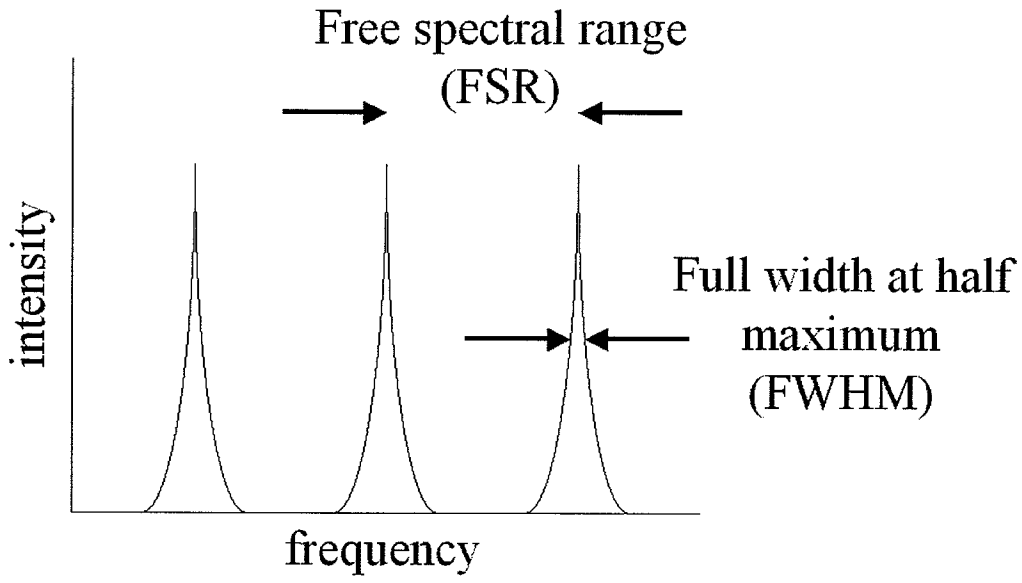

Fig. 2.5. Example plot of transmission of Fabry-Perot etalon for varying frequency.

3. VIRTUALLY IMAGED PHASED ARRAY (VIPA)

3.1 VIPA Construction

The VIPA is constructed in similar fashion to the Fabry-Perot etalon. It too can also be air spaced or solid. The key difference is the input reflective coating. First, it does not cover the entire aperture of the device. A small uncoated or anti-reflective window is fabricated to allow the entrance of a diverging input beam, not a plane wave. This window provides an advantage over the standard etalon. The Fabry-Perot Etalon also performs as a spectral disperser, but the peak transmission depends on the similarity of the reflectivities of the coatings. The VIPA entrance window allows the output power to not be a function of the symmetry of the coating reflectivities, giving it an advantage over the standard etalon. Since a plane wave is not the input to the VIPA and the entrance of the beam into the VIPA is not affected by the input reflective coating, the standard method of analysis that was used with the Fabry-Perot etalon is not valid. Also, since a diverging beam is used, as opposed to a plane wave, diffraction can occur. For example, light can exit the VIPA at a different angle than it entered the VIPA. Secondly, the input coating, or first coating, has a reflectivity as close to 100% as possible. A diagram of the solid and air spaced VIPAs is show in figure 3.1 and 3.2. The VIPA is also not operated with the input beam parallel to the normal of the surface. The VIPA is rotated on its horizontal axis by a certain angle. This allows the insertion of a beam into the cavity which will be reflected back and forth down through the cavity of the VIPA between the reflective surfaces seen in figure 3.3. The varying of the input angle is also one method of controlling the free spectral range of the VIPA. Figure 3.4 shows the input and output angles in relation to the VIPA.

3.2 Previous VIPA Experimentation

The diffraction grating serves as a spectral disperser, but the VIPA has the potential to perform the same function with benefits over the standard grating. A previous experiment to show functionality of the VIPA used a broadband source, a VIPA

to spatially separate the different frequencies, and bare fibers at different locations to observe the output of the VIPA [2]. See figure 3.5 for a diagram of this experimental setup. Data from this experiment shows angular dispersion as show in figure 3.6 by seeing that resonant peaks change when observing at the different locations of the individual bare fibers [2]. Also, the angular dispersion is shown in figure 3.7 by measuring the output angle of the VIPA that certain frequencies can be observed (or constructively interfere) [2]. The output angle of the VIPA is shown in figure 3.8. The functionality of the VIPA is seen in these experiments, but a concrete understanding of the dispersive properties of the VIPA has not been shown. Angular dispersion is explained to have a proportionality to cot(θ), the cotangent of the angle that light is input into the VIPA [2]. Also, the dispersive properties are again indicated in figure 3.7, which demonstrates the dispersive properties also as a function of the angle that light constructively exits VIPA [2]. Since dispersion is a function of the input and output angles that light enter and exit the VIPA, angular dispersion is said to no longer be proportional to only the input angle and be represented by cot(θ). It is said to now be proportional to cot(θ+ϕ/n) [2], where ϕ is the angle that light exits the VIPA. Some type of relation to dispersion of the VIPA is given, but there is no quantitative analysis that leads to this conclusion. A more thorough approach will be presented which will lead to a dispersion law for the VIPA.

3.3 VIPA Theory and dispersion law

3.3.1 Air spaced VIPA

The dispersion law for the VIPA, proposed by Professor Weiner and experimentally tested by myself, was formulated in similar fashion to the analysis of Young's double slit experiment. A bright spot or constructive interference occurs when the difference between two separate path lengths is an integer number of wavelengths or a phase difference of an integer multiple of 2π. The dispersion law for the VIPA that meets the above conditions is given by

$$2tk\left(\frac{1}{\cos(\theta_{input})}\right) - 2tk\left(\tan(\theta_{input})\sin(\theta_{input}+\theta_{output})\right) = 2m\pi \quad (3.1)$$

The condition for constructive interference is a function of the angle that light enters the VIPA and the angle that it exits the VIPA.

In order to derive the dispersion law, we must take a look at the paths that rays of light travel and the angles they enter and exit the VIPA. To begin with, the path length difference that we are concerned with is between path ABC and AD in figure 3.9. The phase acquired from path ABC is

$$k\left(\frac{2t}{\cos(\theta_{input})}\right) \quad (3.2)$$

The propagation constant k is $2\pi/\lambda$ and t is the thickness of the cavity of the VIPA. The phase acquired from path length AD is equal to

$$2tk\left(\tan(\theta_{input})\sin(\theta_{input}+\theta_{output})\right) \quad (3.3)$$

The term $2t*\tan(\theta_{input})$ is the path length AC. With the phase from both path lengths given, the difference must be an integer multiple of 2π radians, giving

$$2tk\left(\frac{1}{\cos(\theta_{input})}\right)-2tk\left(\tan(\theta_{input})\sin(\theta_{input}+\theta_{output})\right)=2m\pi \quad (3.4)$$

This equation is for an air spaced etalon where the angle inside the cavity is the same as the input angle.

The dispersion law also indicates that the VIPA operates as a diffractive device. Constructive interference can occur at different angles from the original angle that light is input into the VIPA.

3.3.2 Solid VIPA

For a solid etalon, we must consider the fact that the internal angle is not the same as the input angle, as seen in figure 3.10. The two are related through Snell's law,

$$\sin(\theta_{input})=n\cdot\sin(\theta_{internal}) \quad (3.5)$$

where n is the index of refraction of the cavity. Now, the phase acquired from path ABC is

$$k\left(\frac{2tn}{\cos(\theta_{internal})}\right) \quad (3.6)$$

and the phase acquired from path AD is

$$2kt\left(\tan(\theta_{internal})\sin(\theta_{input}+\theta_{output})\right) \quad (3.7)$$

The term is adjusted because the path length AC has changed with the internal angle. Both the changes yield

$$2tk\left(\frac{n}{\cos(\theta_{internal})}\right)-2tk\left(\tan(\theta_{internal})\sin(\theta_{input}+\theta_{output})\right)=2m\pi \quad (3.8)$$

The above equation assumes that the index of refraction does not vary or varies too little with the change in frequency. If the index does change with frequency, n would be replaced by n(k) or n(ω/c). Now the phase matching condition depends on the frequency of the input light.

3.4 VIPA Free Spectral Range (FSR)

The relation between the free spectral range and the input/output angles is derived from the dispersion law. The frequency difference between two adjacent orders is known as the FSR. From the dispersion law, the order is set to m and the frequency of one resonant peak is labeled as ν_1. Next, the order is set to m+1 and the frequency of the other resonant peak is labeled as ν_2. Free spectral range is $\nu_2-\nu_1$, and is given by

$$FSR=\frac{c}{2t}\left[\frac{1}{\cos(\theta_{input})}-\tan(\theta_{input})\sin(\theta_{input}+\theta_{output})\right]^{-1} \quad (3.9)$$

Notice that the FSR does not solely depend on a factor of 1/cos(θ) like the Fabry-Perot interferometer does in equation 2.9. For a solid etalon, the FSR is given by

$$FSR=\frac{c}{2t}\left[\frac{n}{\cos(\theta_{internal})}-\tan(\theta_{internal})\sin(\theta_{input}+\theta_{output})\right]^{-1} \quad (3.10)$$

Again the above equation does not take into account that n could change with frequency. If one would want to correctly find the FSR of a solid VIPA where there was a substantial change in index, a type of numerical analysis would be used to find the solutions to eqn 3.10. The difference in frequency between the solutions would be the FSR. The function that would describe the index would be either a Sellmeier equation which attempts to fit index vs. frequency data or a possibly a first order expansion of the index at a certain point given by

$$n(\omega) = n(\omega_0) + (\omega - \omega_0) \cdot \left(\left. \frac{dn(\omega)}{d\omega} \right|_{\omega=\omega_0} \right) \quad (3.11)$$

which is the value of the index at a certain point plus the product of the frequency difference from the point of interest and the first order derivative of the index function with respect to frequency at the point of interest (possibly obtained by two data points of experimental data).

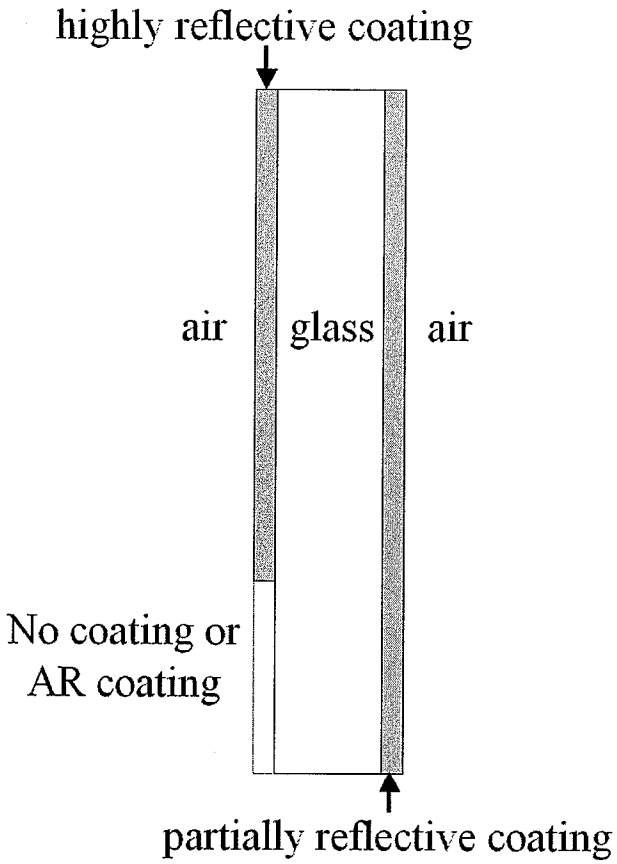

Fig. 3.1. Solid VIPA

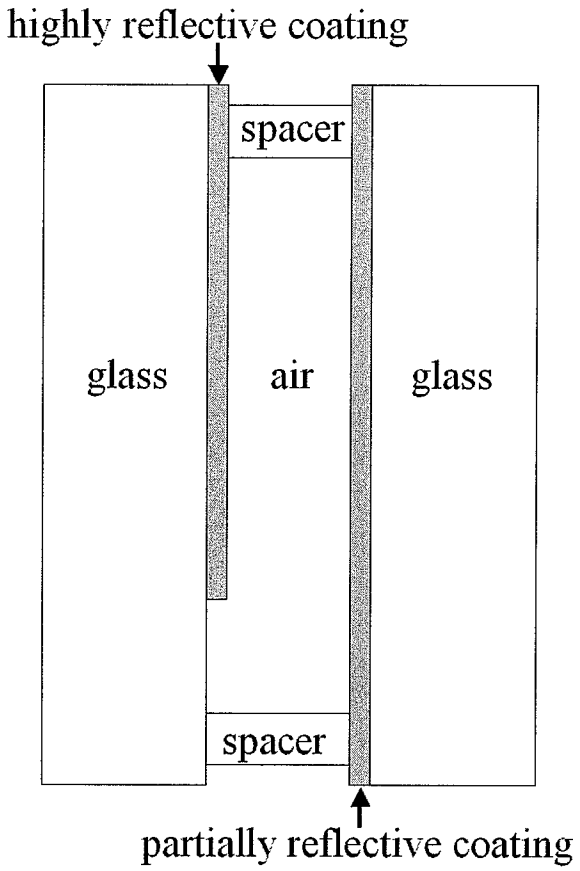

Fig. 3.2. Air spaced VIPA.

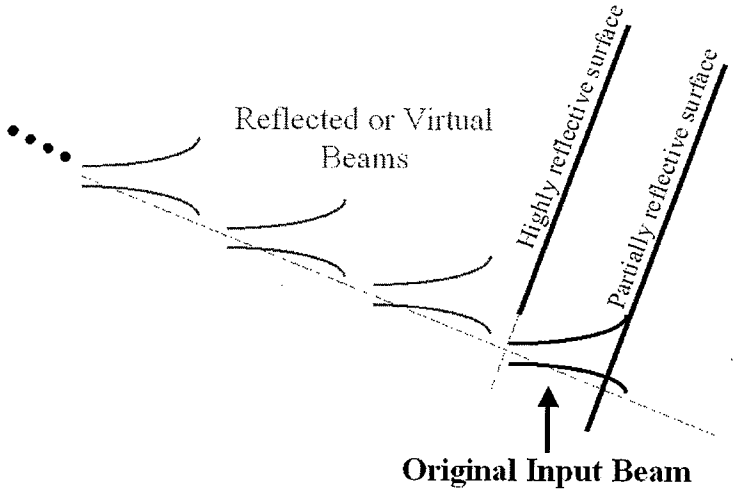

Fig. 3.3. Diagram of input acting as multiple sources.

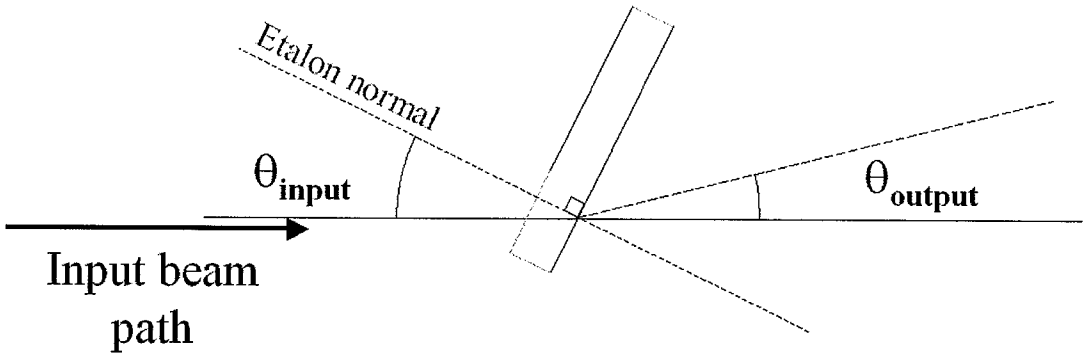

Fig. 3.4. Diagram of VIPA input and output angles.

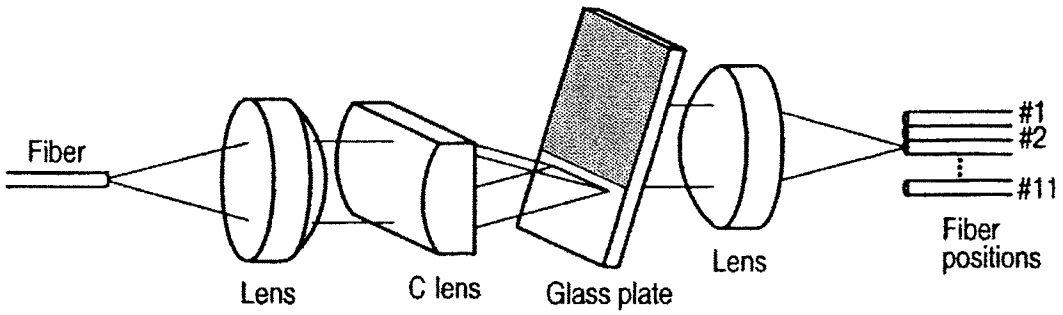

Fig. 3.5 Experimental setup of previous VIPA experimentation [2].

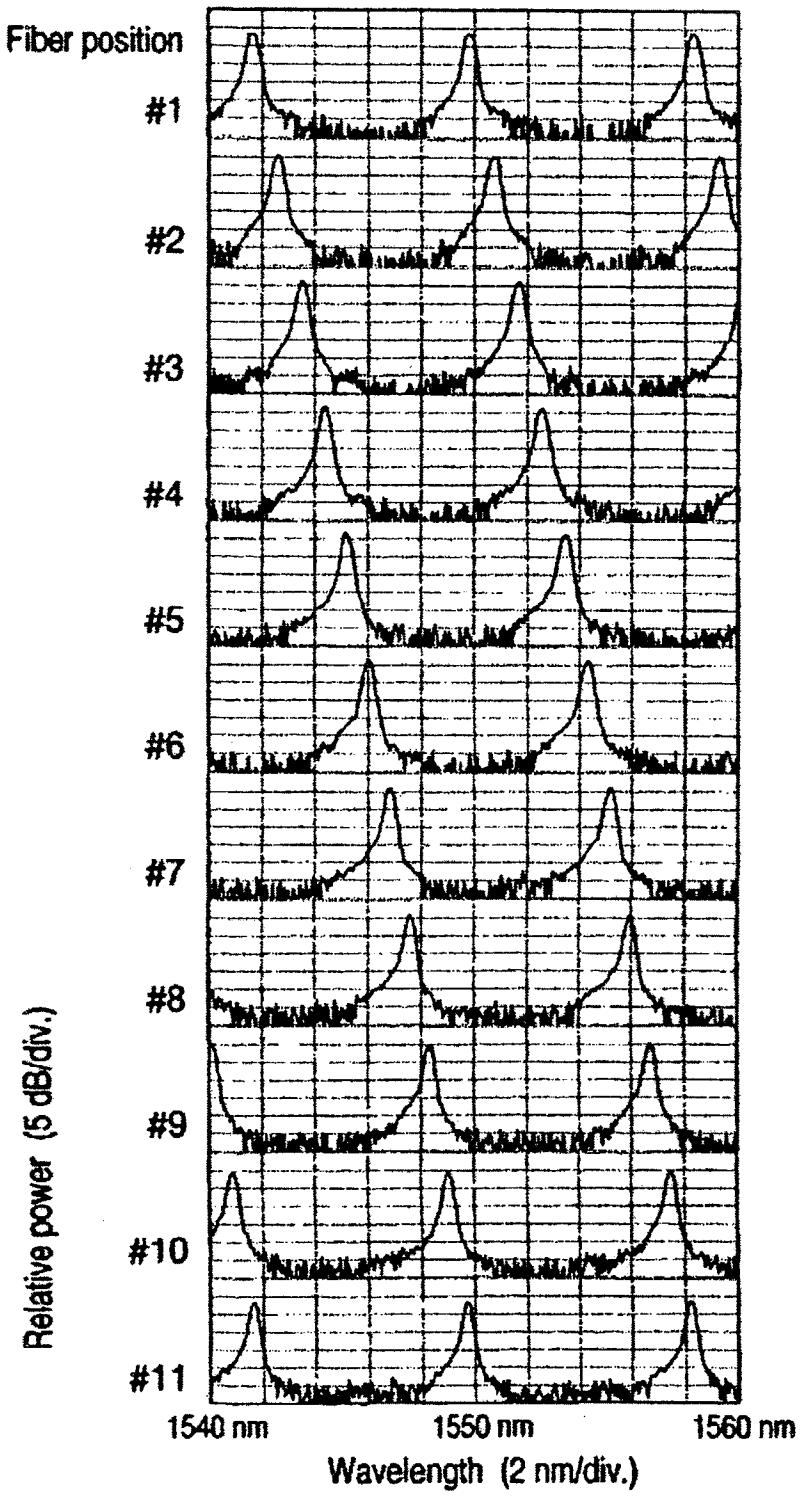

Fig. 3.6. Spectral output for individual fiber positions shown in Fig 3.5 [2].

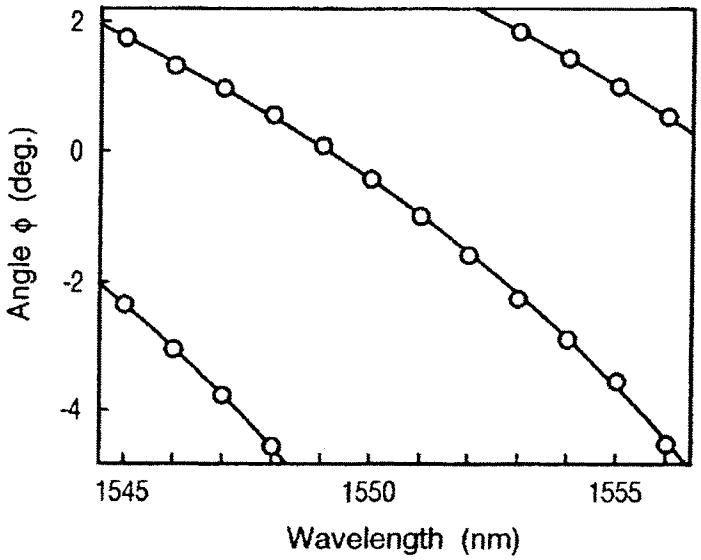

Fig. 3.7. Output angle at which constructive interference occurs for VIPA experimentalization [2].

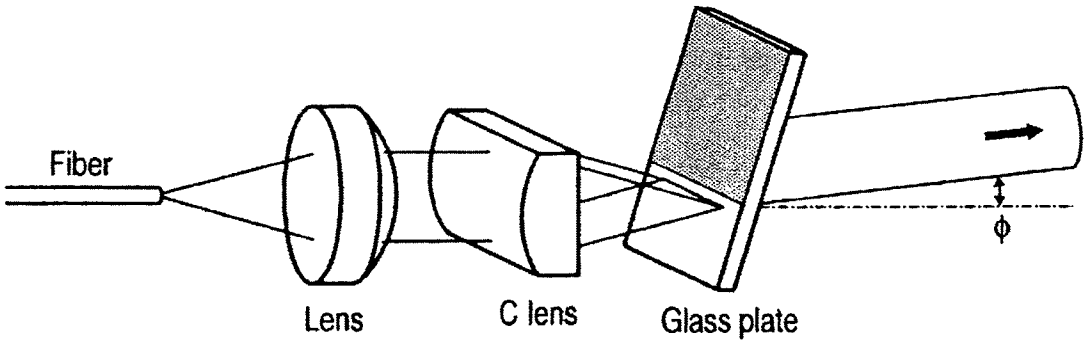

Fig. 3.8. VIPA experimental setup with output angle shown [2].

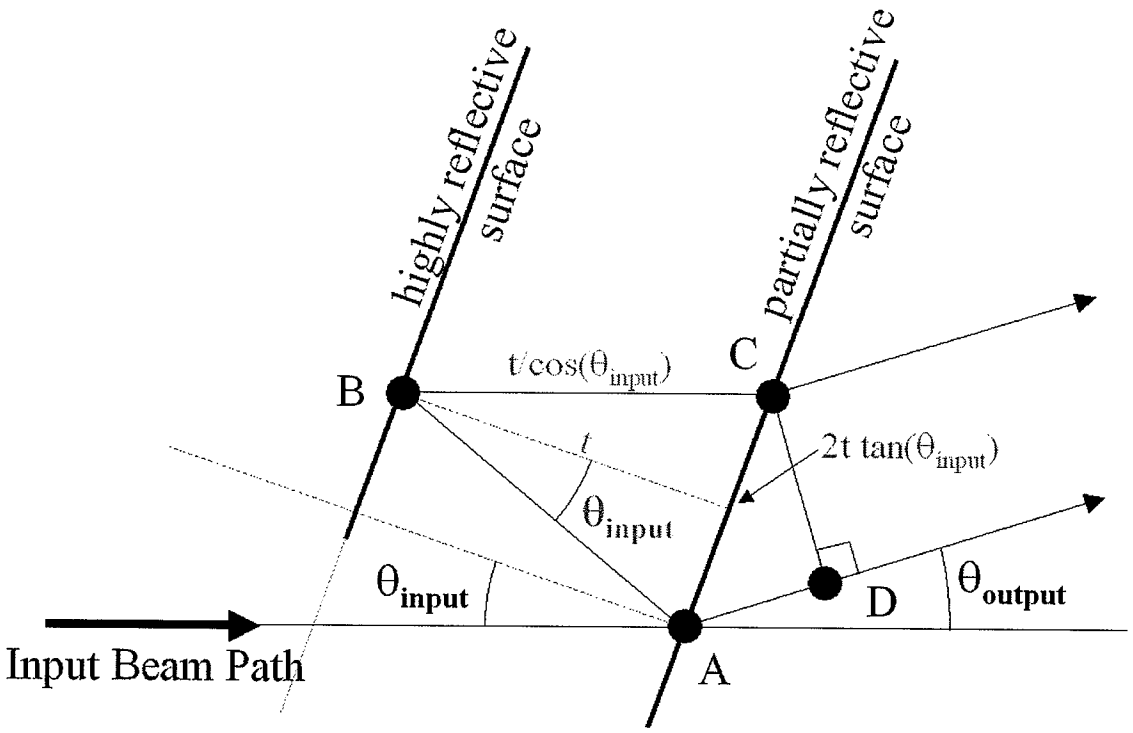

Fig. 3.9. Internal ray paths for air-spaced VIPA.

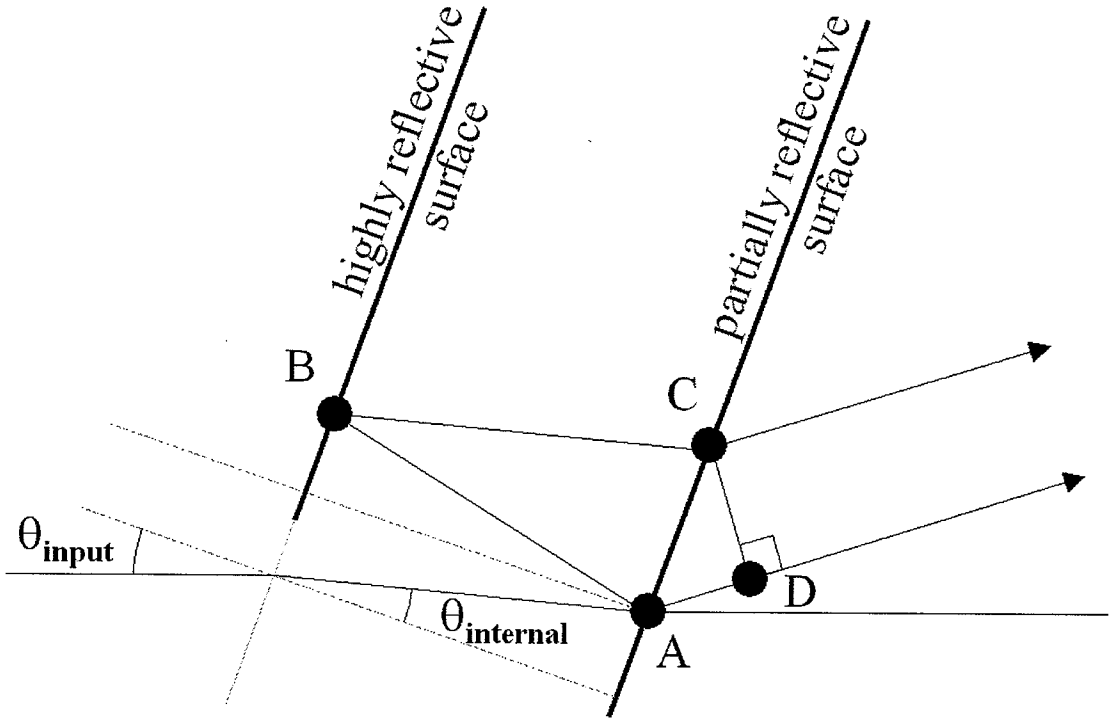

Fig. 3.10. Internal ray paths for solid VIPA.

4. EXPERIMENTAL SETUP

4.1 Introduction

During the experimental portion of this project, three different VIPAs were used. Two VIPAs were air spaced and the third was a solid VIPA. The two air spaced VIPAs were donated by Avanex, a company that provides components for fiber based optical communications. One of the air spaced VIPAs was fixed to a brass mount which also was fiber coupled. The brass mount also contained a gradient index lens (GRIN) to collimate the output of the fiber and a cylindrical lens to focus down the collimated beam into the VIPA at the end of the brass mount. The other air spaced VIPA provided was unmounted and was only the device itself. The solid VIPA was fabricated by TecOptics, a laser optic and etalon provider. It too was also unmounted like the second air spaced VIPA.

The input to any of the three VIPAs was either a broadband amplified spontaneous emission (ASE) source with a usable bandwidth of 1520-1560nm or a tunable laser source which could be tuned from 1510-1650nm. The source that was chosen was either connected to the fiber coupled input of the mounted VIPA or connected to a fiber collimator, with beam size 2.0mm, for insertion into the other two VIPAs. The focused beam size into the VIPA was 9.9μm. This was calculated using

$$w_2 = \frac{\lambda_0 f_L}{\pi w_1} \quad (4.1)$$

where w_2 is the beam radius of the focused spot, f_L is the focal length of the lens, λ_0 is the wavelength, and w_1 is the beam radius of the input collimated beam [5]. For the case of using the unmounted VIPA, a cylindrical lens with a 20mm focal length was used to focus the collimated beam horizontally into the VIPA. The VIPA was positioned on a fine rotation stage to carefully control the input angle. The mounted VIPA already had a collimator and cylindrical lens built into the mount, and had a reported collimated beam size of .5mm after the GRIN lens, a 6.9mm focal length for the cylindrical lens, and focused beam size of 9.2μm. For all VIPAs, an achromatic lens with a focal length of 190mm was placed one focal length from the output surface of the VIPA. This lens is

used to combine the in-phase collimated light exiting the VIPA to a spot one focal length behind the lens, as shown in figure 4.1. On the other side of the lens, also one focal length away, was a bare fiber on a computer controlled translation stage. To convert displacement of the bare fiber into angular displacement out of the VIPA, the relation $\theta_{output}=\tan^{-1}(d_f/f_L)$, where d_f is the displacement of the fiber and f_L is the focal length of the achromat, 190mm. The bare fiber output was connected to either a power meter or an optical spectrum analyzer (OSA). The spectral resolution of the OSA was .01nm. The power meter was used when the input was the tunable source, and the OSA for broadband input. The data from the power meter and OSA were captured by a computer for plotting or analysis. Figure 4.2 shows a diagram of the equipment setup.

4.2 VIPA Specifications

The mounted VIPA has the etalon fixed to a brass mount. The etalons, from Avanex, are made of a material called Dynasile 4000, or an equivalent, and the spacers used to separate the wedges is Zerodur, or an equivalent. Both etalons have anti-reflective (AR) coatings on the outside surfaces of the etalon. On the inside face of the entry wedge of glass, an AR coating covers the clear aperture and the highly reflective dielectric coating covers almost of the clear aperture except for a small window which the input light will be entered into the VIPA. The reflectivity of the highly reflective surface for both Avanex VIPAs is reported to be greater than 99.95%. The highly reflective coating could not be measured because a test beam would have to pass through both reflective coatings. This caused a test beam to be of too low intensity for measurement. On the inside surface of the second wedge, the output wedge, a partially reflective dielectric coating covered the entire clear aperture. The reflectivity of this coating for both devices was reported to be between 97.5-98.0%, but on the unmounted device was measured to be 98.4%. This could be measured due to the highly reflective coating not completely covering the entire aperture. The mounted device could not be measured because the brass fixture did not allow the entrance of a test beam for measuring the reflectivity of the second reflective coating. The outside surface of the second wedge had an AR coating covering the entire surface of the wedge. The thickness for both devices was not specified in the documentation that came with them, but it was determined from data to be .375mm. The mounted device was fixed to the mount at an angle of about 8°. This was determined from rough physical measurements.

The solid VIPA fabricated by TecOptics was constructed of .1mm thick (±.001mm.) Suprasil 2 fused silica and with a 25 mm diameter. An aluminum cell enclosed the device leaving a 20mm diameter clear aperture. The entry side of the etalon was covered with a coating with a reflectivity of >99.5% for wavelengths 1520-1580nm. This coating only covered 75% of the aperture leaving an uncoated window for coupling in the input beam. On the output side of the VIPA, a coating with reflectivity of 97% ±1% for wavelengths 1520-1580nm covered the entire aperture of the device.

4.3 General Observed Output With Narrowband And Broadband Input

4.3.1 Spatial measurements

When a tunable source is used, only at certain angles out of the VIPA constructive interference occurs. This means that for one wavelength there are spots of light at the plane where the bare fiber is positioned. Rays with the same phase are exiting the VIPA parallel to each other and are being focused down to individual spots by the achromatic lens. An example of this is shown by figure 4.3. This measurement is performed scanning the bare fiber along the distance one focal length behind the achromatic lens parallel to the table top surface and recording the intensity by the use of a power meter. The individual peaks are the result of different orders (m = ...,-2,-1,0,1,2...) of equation 3.4 and 3.8. Each peak represents a different θ_{output} angle for which constructive interference occurs.

The intensity pattern at the plane of the bare fiber is different for the use of a broadband source. Instead of having distinct spots, there is one large intensity spot which consists of all the multiple order spots for the different wavelengths of the input source. Figure 4.4 illustrates this.

4.3.2 Spectral measurements

When observing the intensity pattern with the OSA while using the ASE source at a fixed spatial postion, the spectral plot appears very similar to the spectral output of the Fabry-Perot interferometer. There are multiple spectral peaks that are spaced by the FSR of the VIPA within the bandwidth of the source. This occurs because only certain frequencies can constructively interfere at one spot in the observation plane (or exit the VIPA at the same angle). This output is seen for a fixed input and output angle, but if the output angle is slightly changed, the position of the peaks shift in frequency showing that different wavelengths are resonant at different angles, as shown in figure 4.5. Each θ_{output}

measurement was .3 mm apart, or .09 degrees in θ_{output} starting from zero degrees. Also, this result is quite similar to the diffraction grating, where there is a change of output angle for a change of input wavelength.

Taking data with the OSA while the tunable source was used was not performed. There would only be certain angles where the OSA would be able to detect the incoming light, and it would be of only a narrow frequency.

4.4 Avanex Mounted VIPA Experimentation

Testing of the mounted air spaced VIPA was performed before the dispersion law was proposed and this testing was to observe VIPA functionality. Also, since the mounted VIPA has a specific fixed input angle, the dispersion law could not be fully tested on this device. See figure 4.6 to see a picture of the mounted, air spaced VIPA.

Spectral dispersion data was taken from the mounted VIPA using the ASE source and the OSA. At a fixed output angle (or fixed point in the observation plane), spectral data was taken and the resonant frequencies were noted. The bare fiber was moved causing the output angle to change. When the bare fiber was moved, the spectral peaks show on the OSA display would shift in frequency indicating that other frequencies are resonant at different angles. The bare fiber was moved until the same resonant frequencies appeared on the OSA display as those from the first observation point. The same frequencies are resonant, but this is another order (m+1 or m-1, if the m^{th} order was observed in the first case). The total distance that the bare fiber moved in the observation plane was 2.32mm (or .70 degrees in θ_{output}). Since the spectral peak shift, during the total bare fiber movement, resulted in the same resonant frequencies being present, we moved through one FSR. The spectral dispersion results from dividing the change in output degrees by the change in wavelength ($\Delta\theta_{output}/\Delta\lambda$). For the spectral data observed, the FSR was calculated to be 3.22nm or 402.1 GHz, and the resulting spectral dispersion was 0.22 deg/nm. This compares to standard grating which offers 0.09-0.1 deg/nm.

Another form of observing the mounted air spaced VIPA was through imaging. Besides the setup that was shown previously, another simple setup was used to view the intensity profile at the output surface of the VIPA. Figure 4.7 shows the setup. A camera with a tube that responds to light in the 1550nm range was positioned in front of the VIPA and focused to observe the pattern of light out of the VIPA. Figure 4.8 shows an example output of the mounted VIPA with a narrowband laser diode input around 1550 nm. The multiple spots show the VIPA acting as if there are multiple sources.

4.5 Avanex Un-mounted VIPA FSR Experimentation

With the un-mounted, air spaced VIPA, the angle that light is input into the VIPA could be controlled. This was done by placing the VIPA on a mirror mount, which allowed tilt control of the VIPA, and placing the mirror mount on a fine rotation stage to carefully adjust θ_{input}. Figure 4.9 shows a picture of the VIPA positioned on the mirror mount.

Since we now have control over the input/output angles for light entering and exiting the VIPA, the dispersion law can be tested on this device. The input and ouput angles were both swept a range of values and spectral data using the ASE and OSA was captured for every combination of input/output angles. The input angle was varied from 5 degrees to 25 degrees in steps of 5 degrees, and the output angle was varied, once again by moving the bare fiber, from –3 degrees to +3 degrees, in steps of .75 degrees, where the zero degree output angle is the same angle that light enters the VIPA and continues on a straight path.

4.5.1 Spectral data analysis

At every position for a specific $\theta_{input}/\theta_{output}$, the OSA captured spectral data of from the light input into the bare fiber. This data was then extracted by a computer to be analyzed by a Matlab script. The script evaluated each peak in the data and compared it to an adjacent peak. The wavenumber difference between the two peaks was used to produce the FSR, where the wavenumber is defined as $2\pi/\lambda$.

4.5.2 Spectral data/FSR results

The FSR data for the air spaced etalon is show in figure 4.10. The actual data points are represented by open circles and the theoretical values given by solving equation 3.9 are represented by the solid lines. The data points are in excellent agreement with the theoretical values showing the accuracy of the dispersion law.

4.5.3 Thickness calculation

The thickness of the VIPA could be determined by rotating the VIPA to zero degrees and the FSR would be a relation of the cavity thickness. A zero degree measurement could not be performed with the VIPA since light is supposed to reflect through the length of the device and some minimal input angle is needed for the input

beam to perform like this. If a zero degree input angle was chosen by entering a beam through the first reflective coating and not through the window available for standard VIPA operation, the intensity of the transmitted light would be very low because of the very high reflectivity of the first reflective coating and the highly reflectivity of the second coating.

Since a measurement is not possible, a type of curve fitting was used to determine the FSR at zero degrees. Theoretical data for the FSR of the VIPA shows that for any θ_{output} value, the FSR should equal one value (c/2d) when $\theta_{input} = 0$. See figure 4.11 for an illustration. A second order polynomial was fit was made to each set of data taken from 5 to 25 degrees for the input angle for one specific θ_{output} value, as shown in figure 4.12. Now, a curve estimates the value of the FSR at $\theta_{input} = 0$ for a certain output angle, and the FSR was calculated by averaging the FSR values given by each curve fit for each different θ_{output} values. The value of the thickness for the air spaced, un-mounted VIPA is again related to the FSR at $\theta_{input}=0$, and was calculated to be 0.3738mm.

4.5.4 Input/output angle and thickness fitting

When the data taking procedure was completed and the very first graph like figure 4.10 was created, the data and the theoretical values matched trends and looked like the theoretical values, but were shifted in certain directions. This original shift caused a look into the accuracy of the values of the input and output angles. The question was if we knew exactly what input angle the beam was inserted into the VIPA or exactly the output angle from which light exited the VIPA.

For the input angle, relative movements from one angle to another were precise due to the fine rotation stage, but the exact location of the zero degree mark was unknown. This was caused by attaching the VIPA at an arbitrary angle to a tilt platform which itself was placed on the rotation stage at some angle. An estimate of the zero input angle was determined by observing the output light of the VIPA with the same infrared camera used in the imaging of the mounted VIPA. The estimated zero degree point was determined by observing the angles where light only went straight through the VIPA and when it produced reflections along the output face.

The above mentioned method proved to not be the best procedure and a simple experiment was needed to confirm the offset in input angle. A laser source in the same plane of the achromatic lens and a measured distance from the zero output angle axis was incident on the output surface of the VIPA, seen in figure 4.13. The reflection of the laser source would appear in the same plane at the exact distance away from the center

axis if the VIPA was at its true zero degree point. From a rough measurement the VIPA was displaced from its correct angle by an estimated 1.1 degrees. If the experimental data was shifted by 1.1 degrees to the correct position, the aligning of the theory curves with the experimental data would be in better agreement. Even with a shift of 1.1 degrees, there was room for more improvement. By shifting the data by a total of 1.4 degrees, there was excellent agreement. Noting that from the final shift value, accuracy of determining the zero degree point would be <2 degrees using the infrared camera, and <0.5 degrees using the simple setup in figure 4.13.

If a single ray entered the VIPA at a certain angle and continued to pass straight thought the VIPA without experiencing any reflections, that ray would exit the VIPA at the angle $\theta_{output}=0$. This zero value output angle would be the same angle as the input angle. When data was taken at a certain output angle, the measurements were taken at relative θ_{output} angles. The determination of the zero output angle was performed by removing the VIPA from it position behind the cylindrical lens and observing the location of the center of the intensity spot in the plane of the bare fiber. As with the input angle, the data was also fitted for the output angle. The data was shifted to fit the theoretical curve, and the amount shifted was 0.15 degrees. This leads to an uncertainty of < 0.2 degrees for determining the zero value of the output angle.

In producing the plot in figure 4.10. the thickness used to calculate the FSR was adjusted to fit the data. The thickness that was used to produce the theoretical curves was 375.0 μm. The uncertainty of determining the thickness of the VIPA is roughly determined from the difference between the thickness calculated by the FSR and the thickness used above to plot the theory curves. This yields an uncertainty of <1.5μm of 0.4% of the device thickness.

4.5.5 Data uncertainty

When taking and analyzing data, a number of occurrences could cause errors in determining the FSR of a device. A few of these aspects were investigated to see their effect on accuracy with regards to the theoretical prediction.

When the spectral data was analyzed, each of the spectral peaks was detected and the FSR was calculated from averaging the observed frequency difference between each peak and the next lower frequency peak. Some of the data taken had peaks, which were also used to determine the FSR, at the edge of the bandwidth of the source. These peaks had less power than other peaks that were closer to the center frequency of the ASE

source. This lower power could result in an inaccurate determination of the center of that peak and cause an error in calculating the FSR. Since the FSR is an average of a frequency difference for a few sets of peaks, an incorrect value for only one set of peaks causes makes the result more sensitive to small errors. In order to compensate for this, the FSR is calculated from averaging the frequency difference between all possible different combinations of sets of spectral peaks. Figure 4.14 shows a comparison of the FSR for the air-spaced, un-mounted Avanex VIPA with only a simple average and the average of all the combinations of the sets of spectral peaks. The simple average is shown in the dotted line and the combinational average is show with the solid line. The dotted line shows some variation on the 13.6 degree input angle and the solid line tends to produce a less jagged results and it follows the trend that is expected from the dispersion law. The variations in the FSR using the simple average did not occur all the time, but the combinational average was used to ensure a more accurate FSR when these errors did occur.

Another source of error could come from inaccurately determining where the peaks are in the presence of noise. The program that calculated the FSR by observing a set of peaks looked for the highest point on a peak. If the noise level was high enough or if the data curve was jagged, the highest point on a spectral peak might not represent the center of the peak. See figure 4.15 for an example of this. To see if this affected the calculation of the FSR, another program was written to fit a polynomial to the spectral data and the peak of the polynomial was used as the center of the peak. Also see figure 4.15 for an illustration. Once the center of the peak was determined, the same process described previously was used to calculate the FSR. The curve fitting to the peak proved to be not necessary. The FSR calculated using the curve fitting offered a slight advantage over the FSR provided by the simple average, where the two are compared in figure 4.16, but the FSR calculated by the combinational average provided the best results over the curve fitting data, see figure 4.17. The large amount of averaging in the combinational method could possibly filter some of the errors the curve fitting was intended to correct.

The last source of error that was investigated was human error and mechanical movement error. The input angle for light into the VIPA is controlled by physically manipulating a rotation stage, and the output angle is controlled mechanical translation stage. To test for these errors, multiple sets of spectral data was taken at different time intervals and after adjusting the various angles associated with the VIPA. The FSR was then calculated to see if any changes occurred. Figure 4.18 shows three sets of data taken for the air-spaced, un-mounted Avanex VIPA with an input angle of 11.1 degrees. The

first set of data was taken, and the second set was taken after three weeks of the first set and after adjusting the input and output angles multiple times. The third set of data was taken one week after the second after only adjusting the output angle with the translation stage. The three data sets are very close to each other and indicate no problem in repeatability.

4.6 Solid VIPA Experimentation

The solid VIPA from TecOptics was tested in a similar fashion to that of the air-spaced, unmounted Avanex VIPA. With the solid VIPA, shown in figure 4.19, the input/output angles were also able to be controlled, and the same data was taken. The only difference is that spectral data was not taken for the solid VIPA at $\theta_{input} = 5$ degrees. At this input angle, the input beam was too large for the 100μm thickness of the device. With such shallow angles, the reflection off the second partially reflective coating returning to the first highly reflective coating would not completely land on the first coating. Part of the reflected beam would land on the window that is used for inserting the beam, and that part of the reflection would be lost. From the data that was taken in these measurements, and using the data analysis method described in the previous subsections, FSR data was calculated from the spectral data. Figure 4.20 shows the data and the theoretical curves, where the circles represent data and the solid lines represent the theoretical values. This device also shows great agreement with the theoretical prediction, and shows that the theory applies to both types of devices and is not limited to device construction conditions.

The thickness of this device was also calculated from the data using the same method of curve fitting to the data. Since with the solid VIPA, spectral data could not be obtained at less than $\theta_{input} = 10$ degrees, the accuracy of the estimation of the FSR would not be as great when compared to the air-spaced VIPA. The closer the data points get to the zero degree input angle, the better the curve fit which allows a better FSR estimate. The calculated thickness of the VIPA from the FSR data is 102.9μm.

With the solid VIPA, a much more thorough setup method was performed to obtain a better value of both the input and output angle zero values. During setup, the center point of the collimated beam in the observation plane was noted, before the insertion of other optics or the VIPA, in order to determine the zero value for the output angle. Also, when mounting the VIPA to the fine rotation stage, the simple setup using an extra laser and reflecting it off the face of the VIPA was used to determine the zero

value of the input angle. With this improved setup method, no fitting for either the input or output angles was needed.

The only fit that was necessary was for the thickness. Since the estimation of the thickness was rough because of the lack of data points near the zero input angle, the device thickness that was used to produce the theoretical curve in figure 4.20 was 102.75 μm. The difference of the two values yields an uncertainty of < 0.2 μm, or .2% of the thickness.

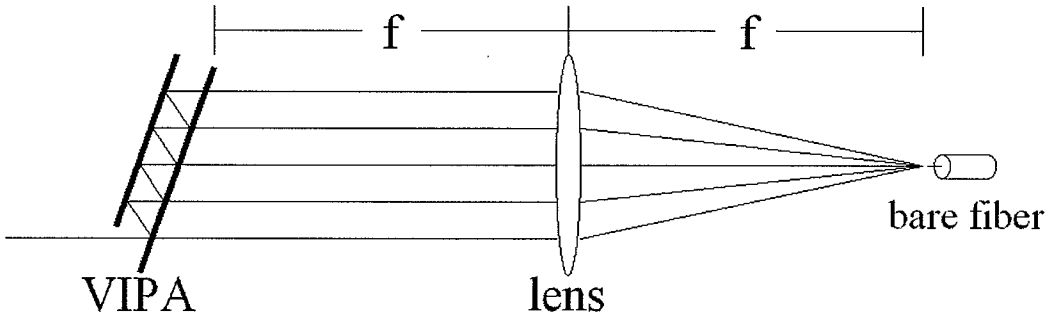

Fig 4.1. Diagram of the constructive light exiting the VIPA and the function of the lens one focal length behind the VIPA performs.

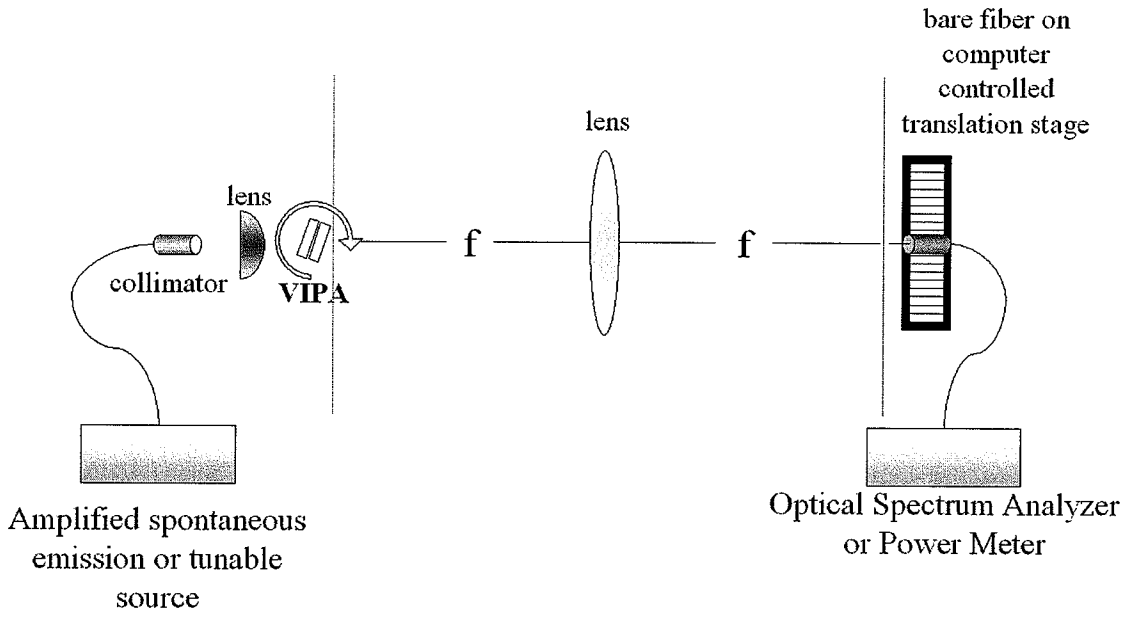

Fig 4.2. Experimental setup used for the un-mounted, air-spaced Avanex VIPA and the solid TecOptics devices.

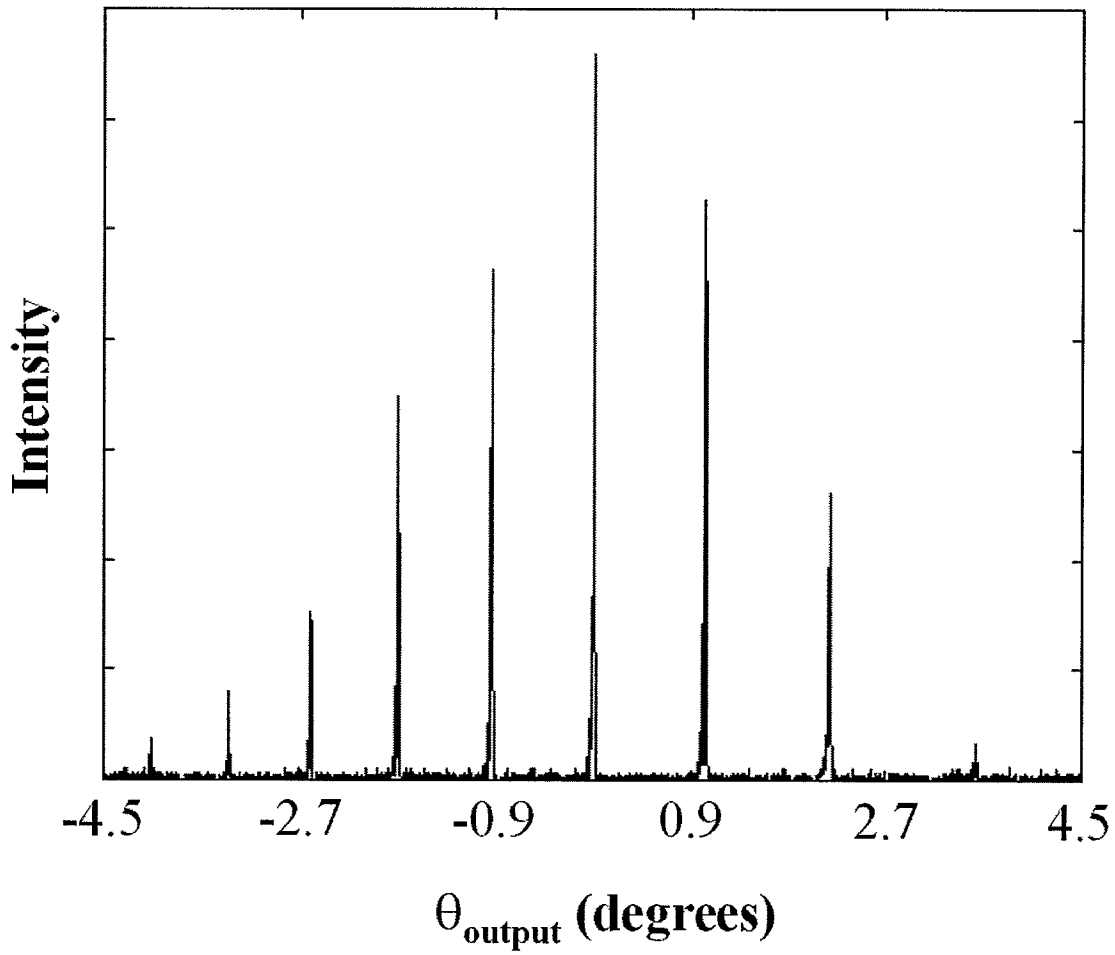

Fig. 4.3. Spatial output intensity profile of the un-mounted, air-spaced Avanex VIPA in plane with bare fiber detector using a monochromatic source at 1550nm and an input angle of 8.6 degrees.

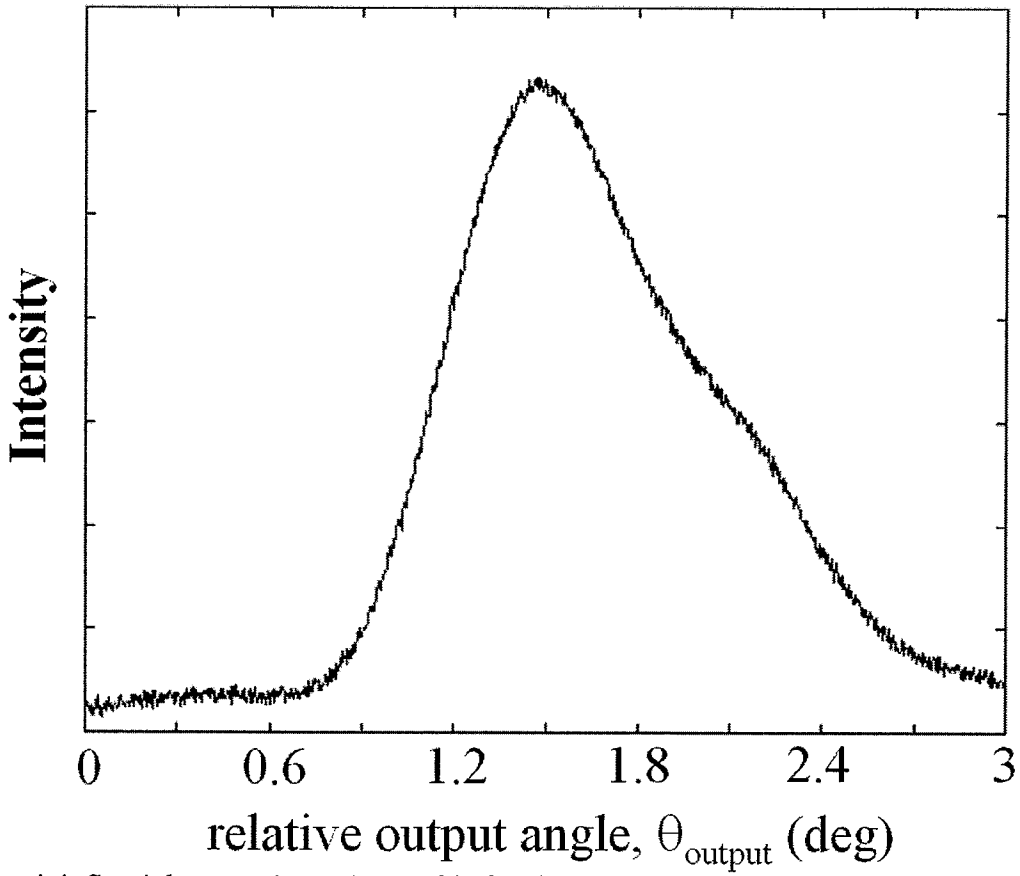

Fig. 4.4. Spatial output intensity profile for the mounted, air-spaced VIPA from Avanex in plane with bare fiber detector using the ASE source.

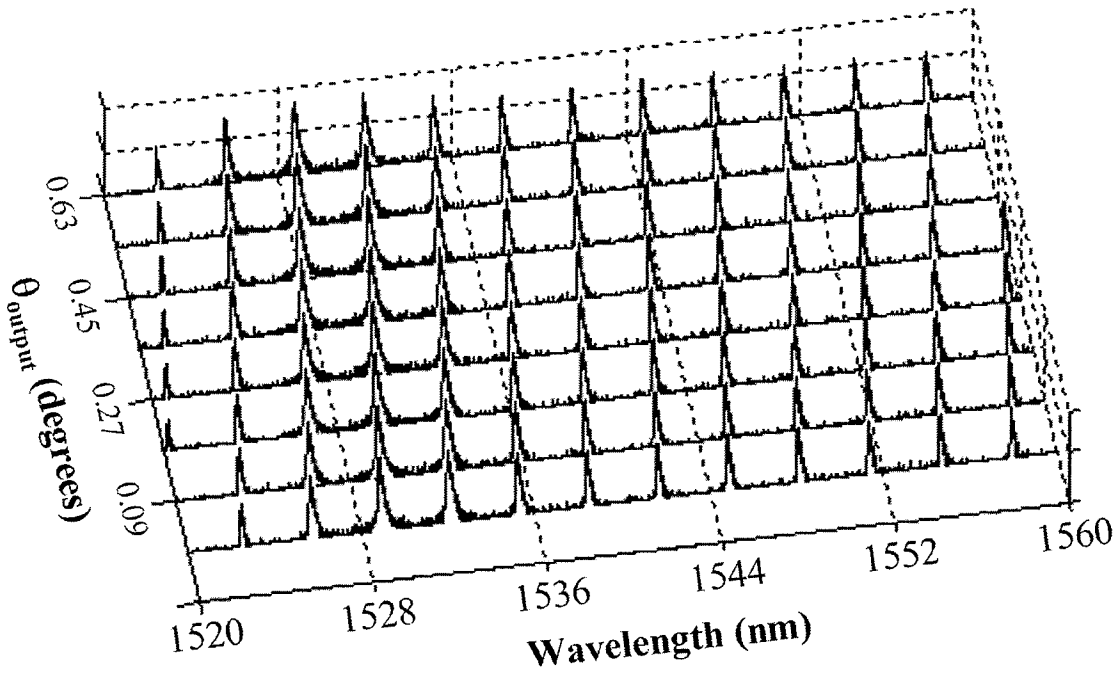

Fig. 4.5. Spectral output for the un-mounted, air-spaced Avanex VIPA in plane with bare fiber for different output angles using the ASE source and an input angle of 11.1 degrees.

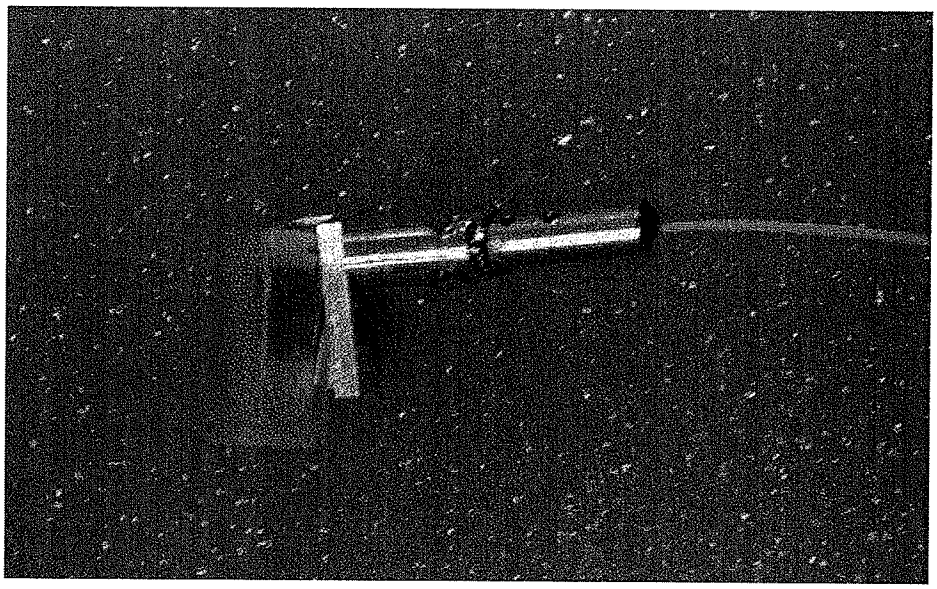

Fig. 4.6. Picture of the air-spaced, mounted Avanex VIPA.

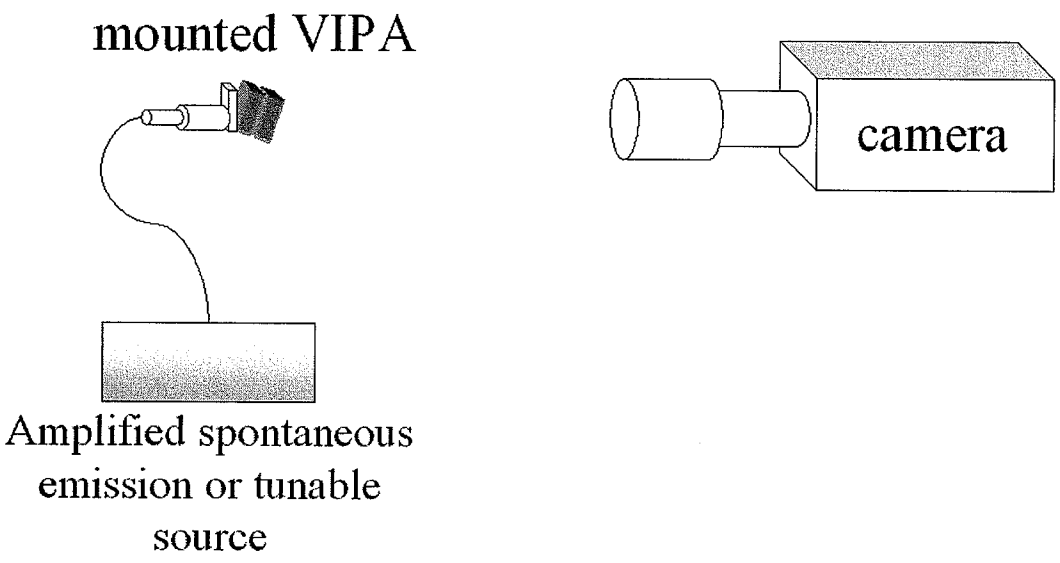

Fig. 4.7. Infrared camera setup used to observe the light at the output face of the air-spaced, mounted VIPA from Avanex.

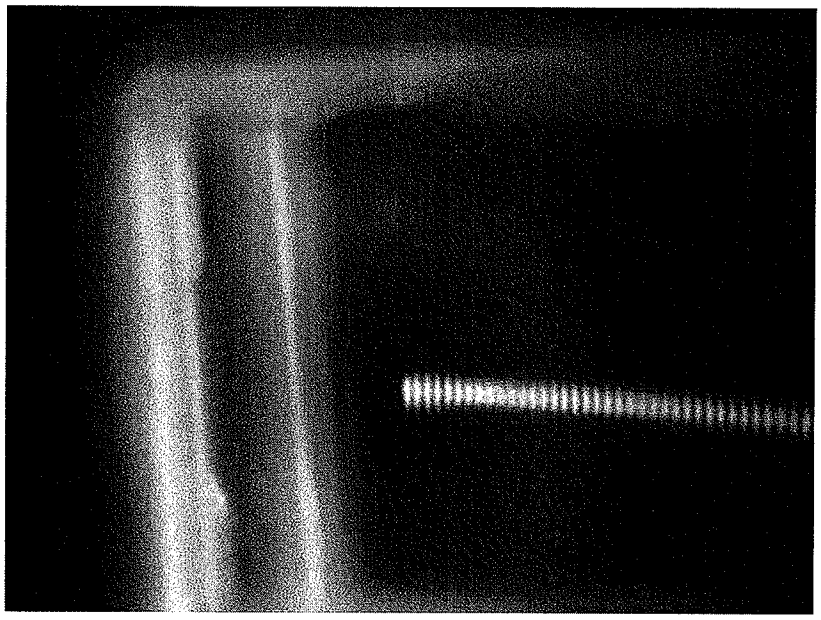

Fig. 4.8. Output light at the output surface of the air-spaced, mounted VIPA from Avanex using the infrared camera setup and a 1550nm source.

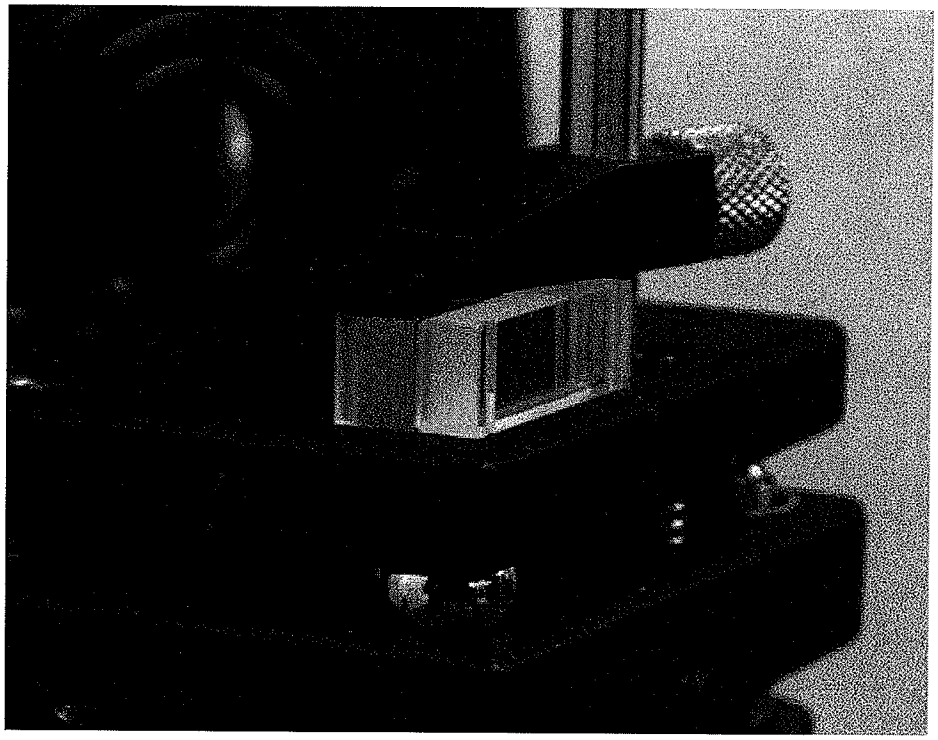

Fig. 4.9. Picture of .375mm air-spaced, un-mounted VIPA from Avanex.

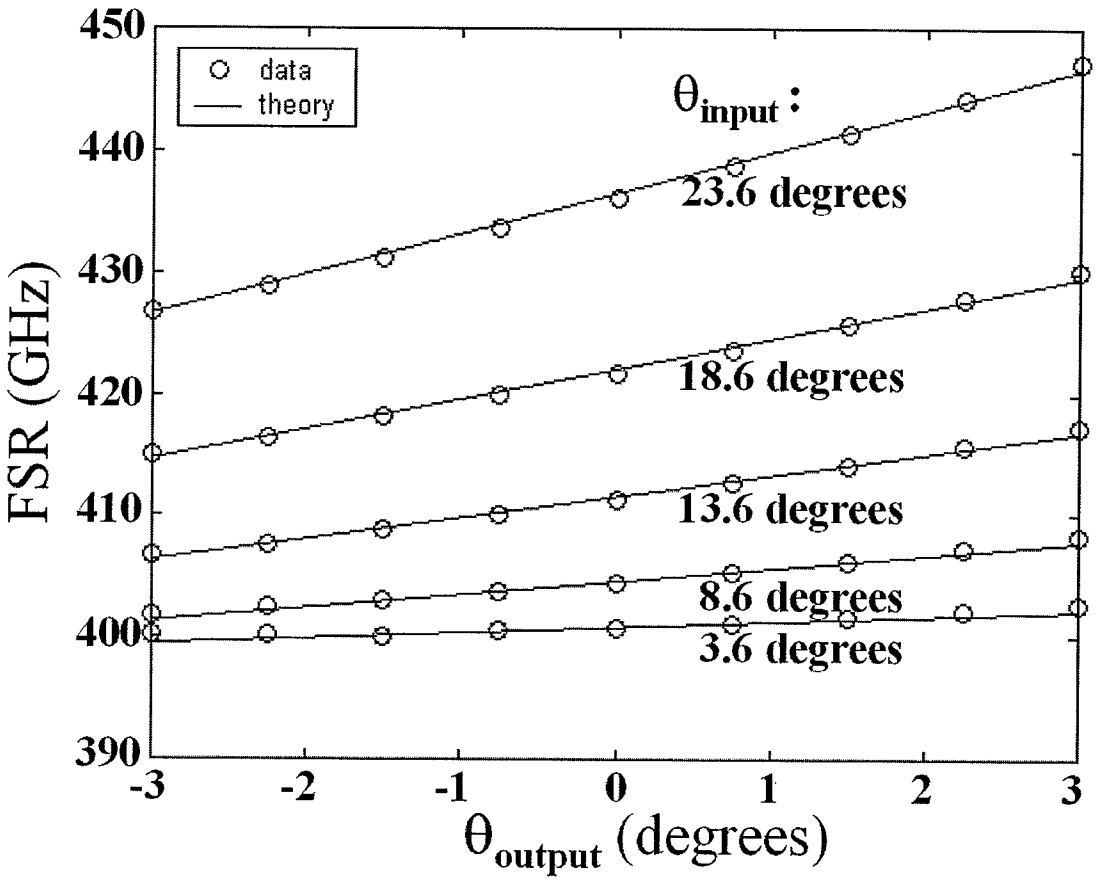

Fig. 4.10. FSR of .375mm air-spaced, un-mounted VIPA from Avanex compared with theory.

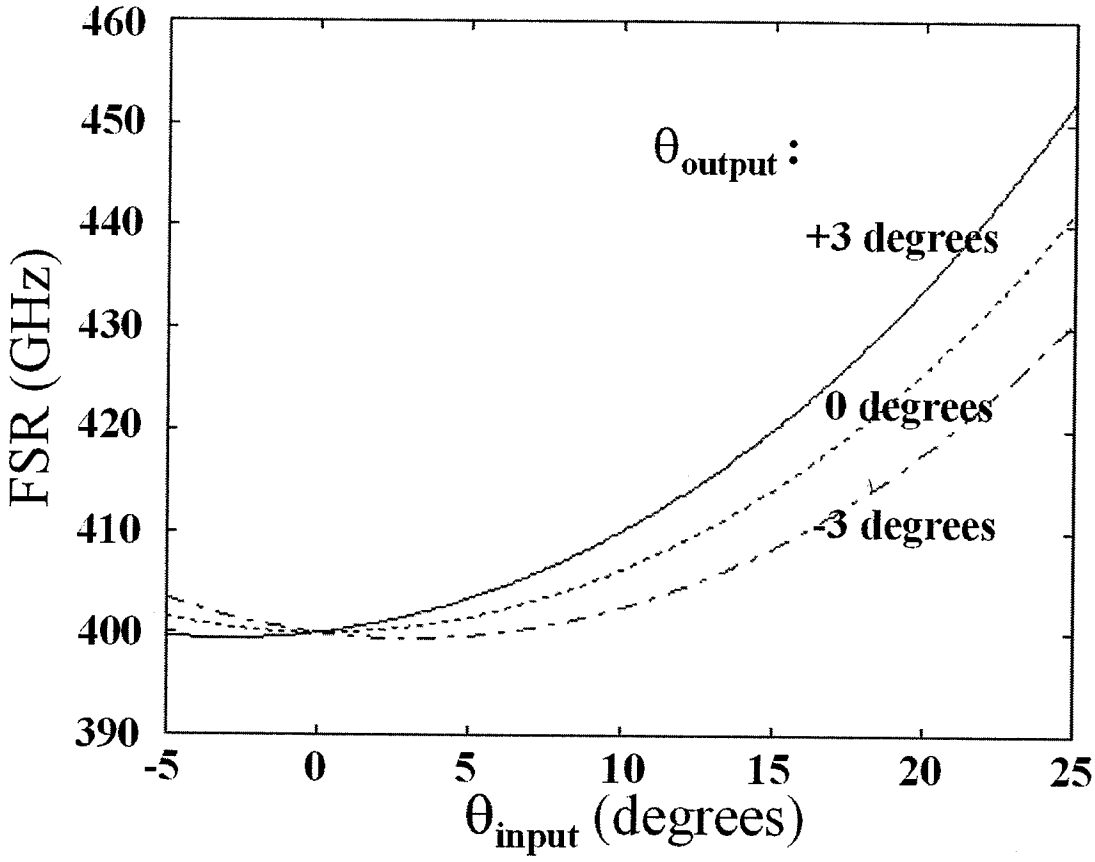

Fig. 4.11. Plot of theoretical curves of the FSR through a range of input angles.

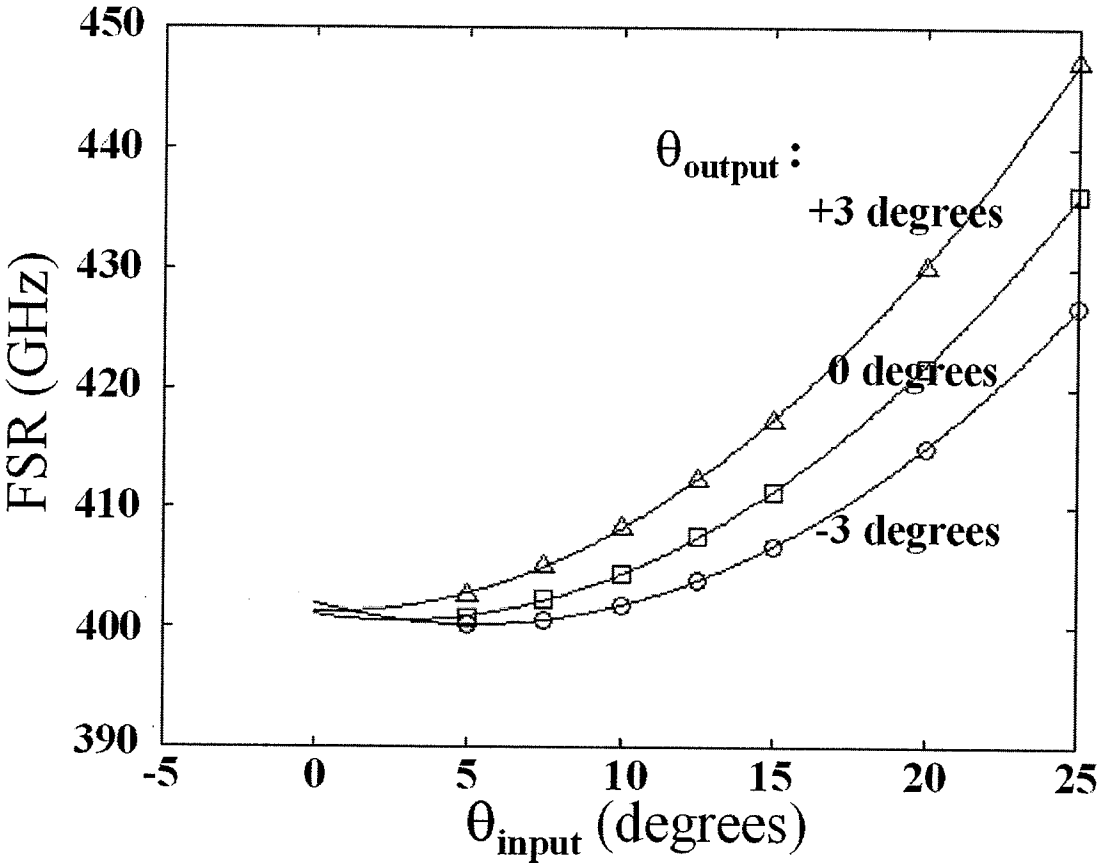

Fig. 4.12. Plot of curve fitting to the data for the air-spaced, un-mounted Avanex VIPA for thickness estimation.

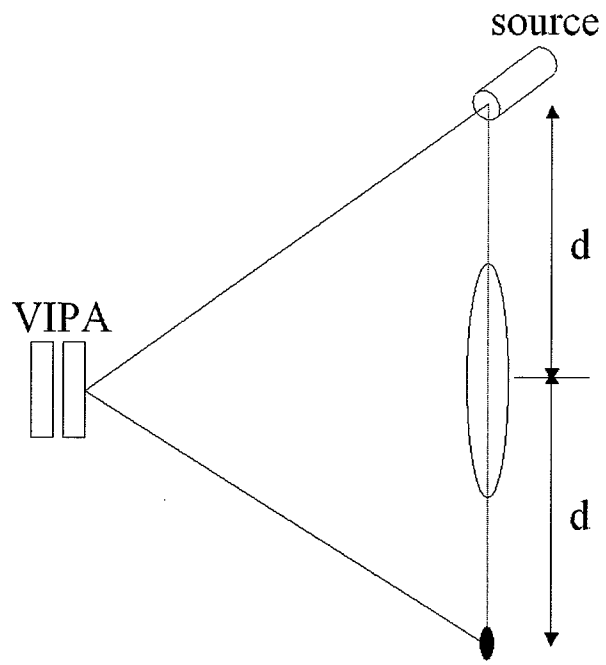

Fig. 4.13. Setup using laser source to determine zero VIPA angle for Avanex air-spaced, un-mounted and solid TecOptics devices.

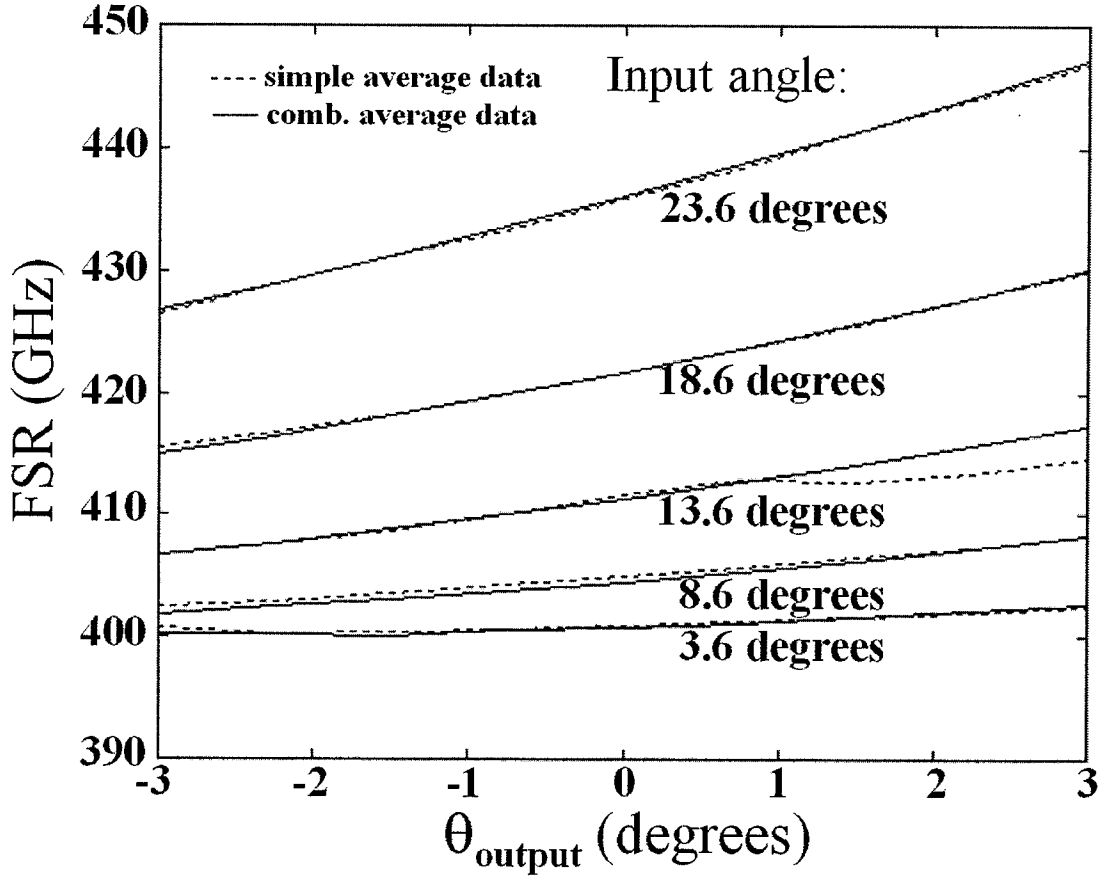

Fig. 4.14. Comparison of FSR for simple average data to combinational average data for air-spaced, un-mounted Avanex VIPA.

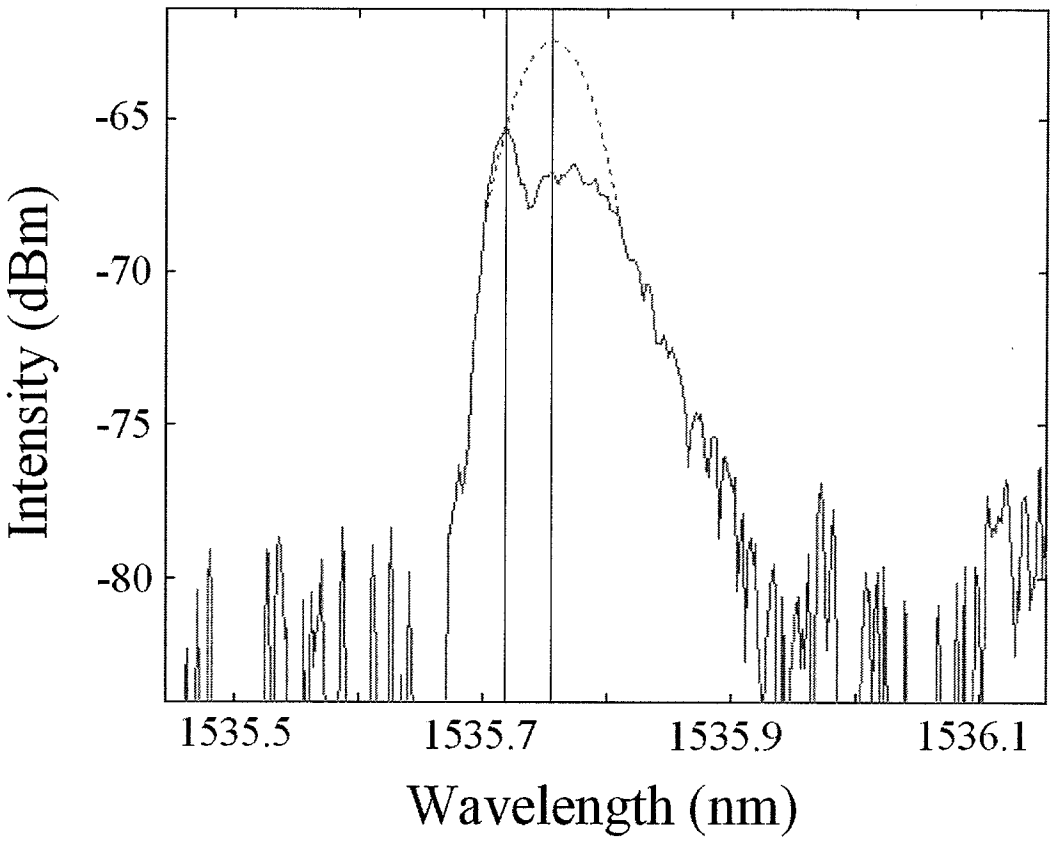

Fig. 4.15. Plot of spectral peak with vertical markers showing the maximum value of the peak and the maximum value of a curve fit to more accurately determine the center of the peak. This data is taken from the air-spaced, un-mounted Avanex VIPA with an input angle of 6.1 degrees and an output angle of -3.0 degrees.

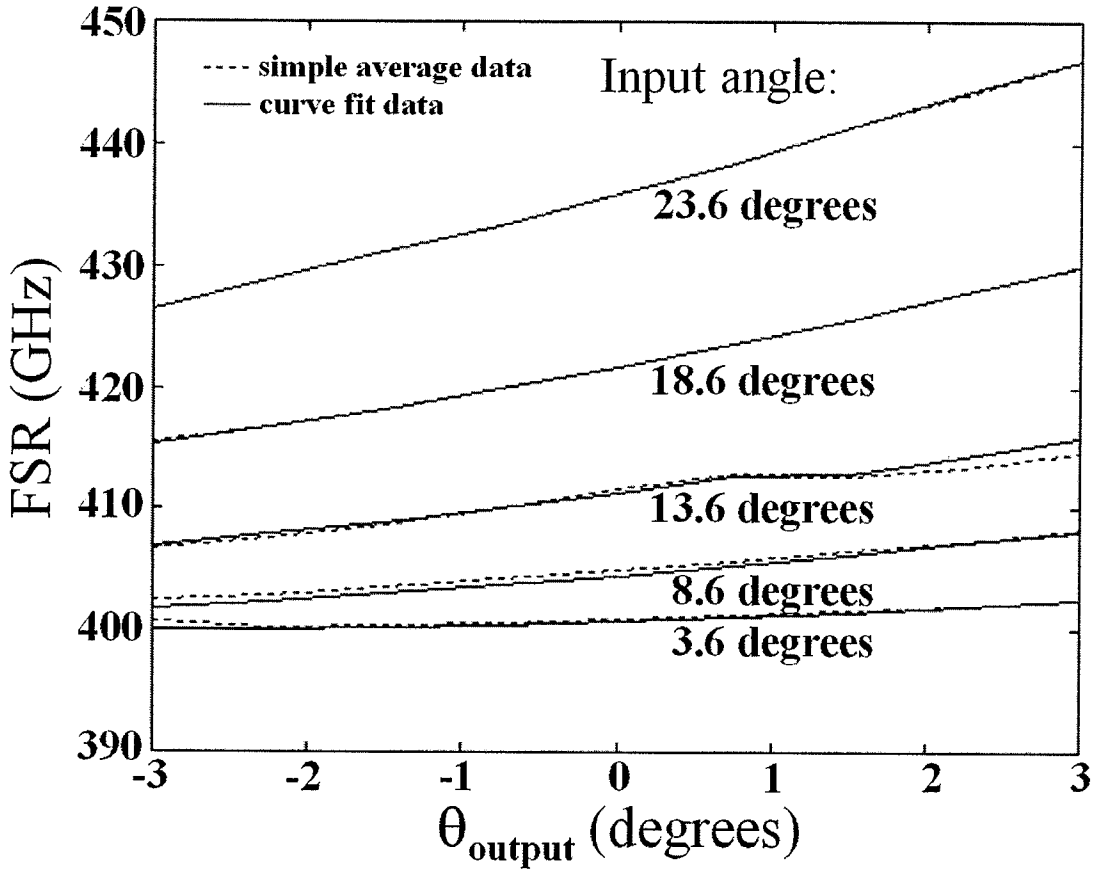

Fig. 4.16. Comparison of FSR for simple average data to curve fit data for air-spaced, un-mounted Avanex VIPA.

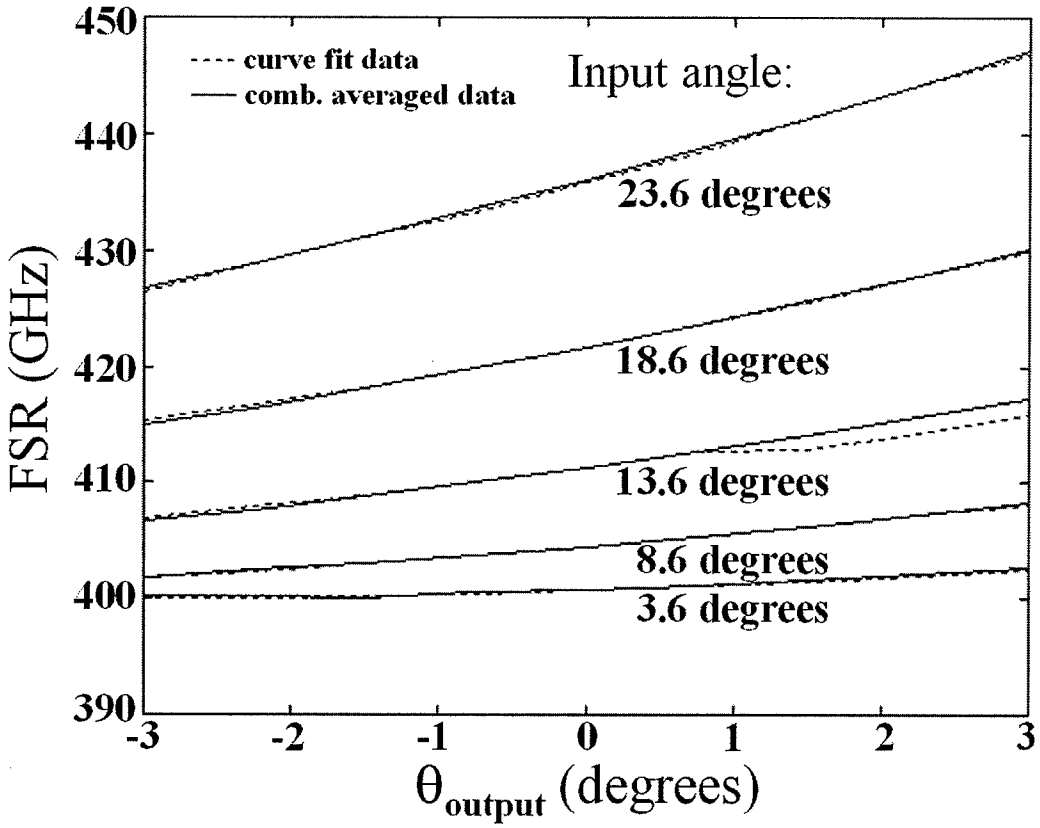

Fig. 4.17. Comparison of FSR for combinational average data to curve fit data for air-spaced, un-mounted Avanex VIPA.

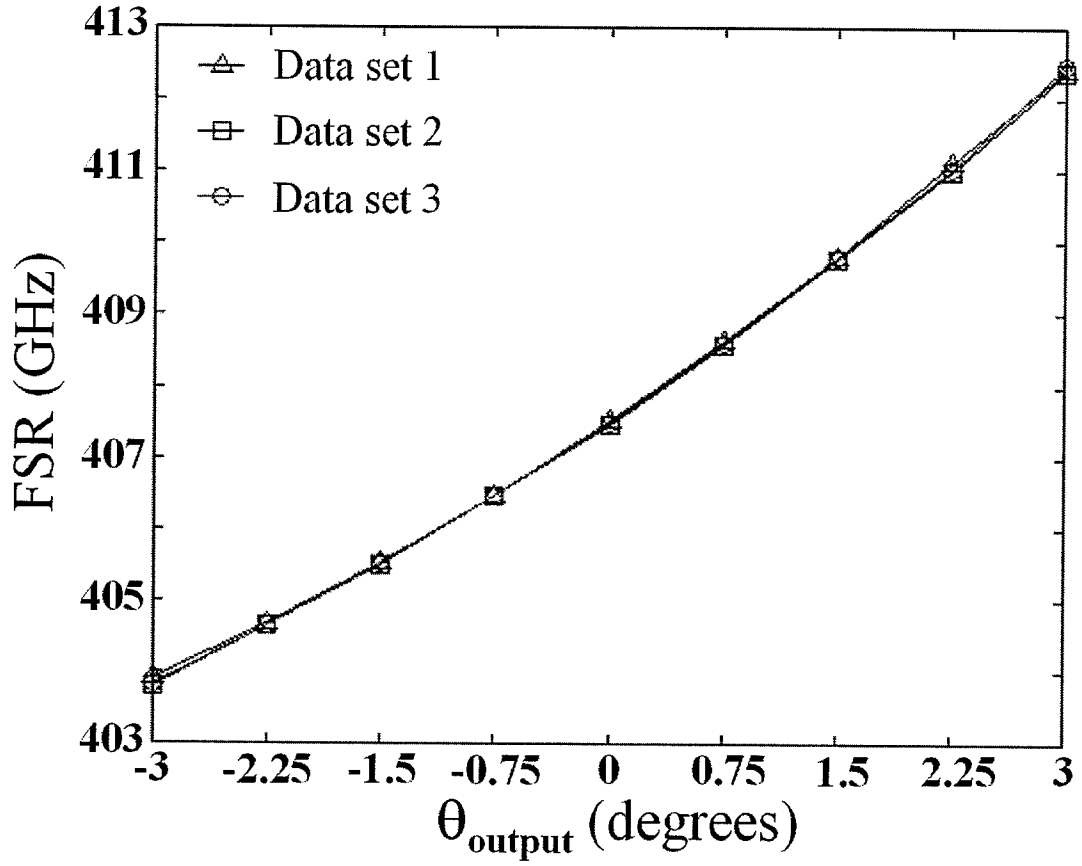

Fig. 4.18. Repeatability data for un-mounted, air-spaced Avanex VIPA with input angle of 11.1 degrees.

Fig. 4.19. Picture of solid VIPA from TecOptics.

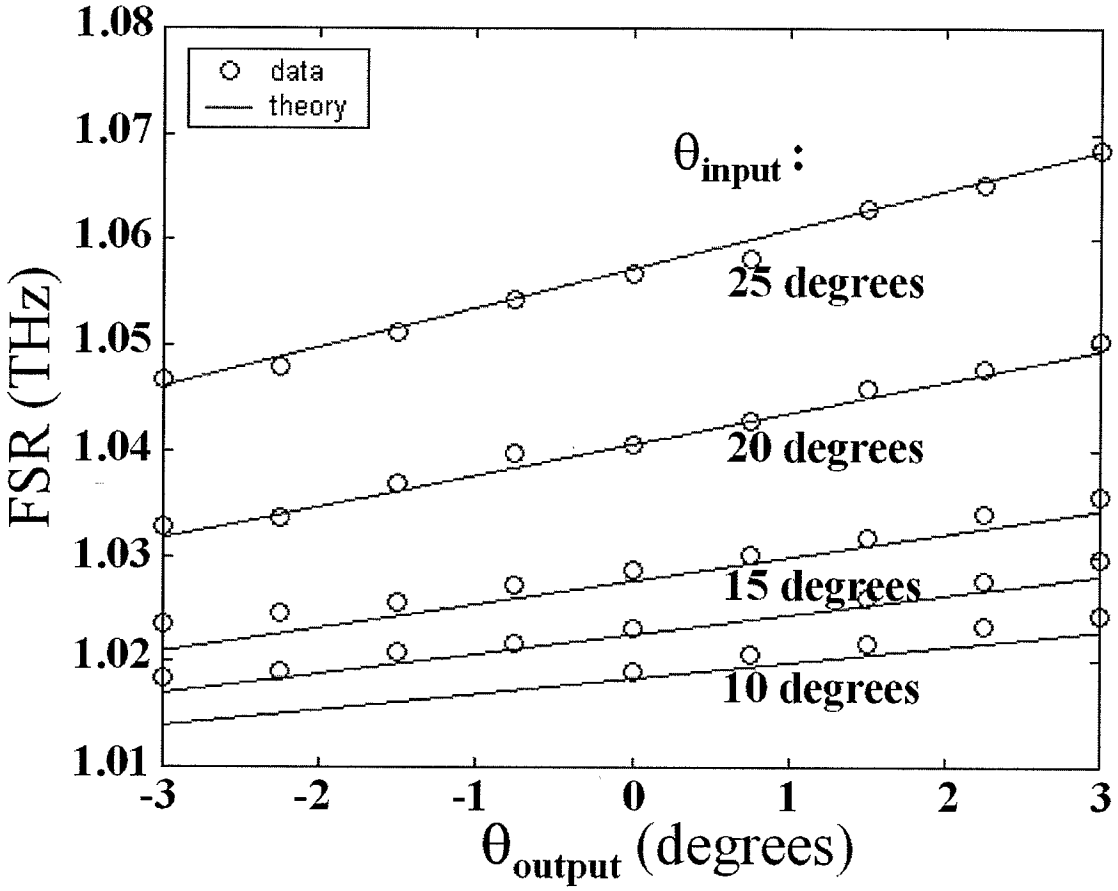

Fig. 4.20. FSR of 100μm solid VIPA from TecOptics compared with theory.

5. CONCLUSION AND FUTURE WORK

To summarize this thesis, the Virtually Image Phased Array has become another device for spectral dispersion. Its effectiveness has been proved, but in this thesis a dispersion law was proposed for the first time and verified experimentally. The accuracy of the dispersion law was shown through free spectral range measurements to be in great agreement with the theory. This theory was also proved again through an alternate solid VIPA provided from another source.

Future work consists of observing losses from reinserting signals back into the VIPA after reflecting off a mirror and alignment concern on the path to dispersion compensation and/or pulse shaping using a liquid crystal modulator and mirror.

LIST OF REFERENCES

[1] M. Shirasaki, A. N. Akhter, and C.Lin, "Virtually Imaged Phased Array with Graded Reflectivity," IEEE Phot. Tech. Lett. **11,** 1443-1445 (1999).

[2] M. Shirasaki, "Large angular dispersion by a virtually imaged phased array and its application to a wavelength demultiplexer," Opt. Lett. **21,** 366-368 (1996).

[3] M. Shirasaki, S. Cao, "Compensation of chromatic dispersion and dispersion slope using a virtually imaged phased array," in OSA Trends in Optics and Photonics (TOPS) Vol 54, Optical Fiber Communication Conference, Technical Digest, Postconference Edition (Optical Society of America, Washington DC 2001), TuS1 pp 1- 3

[4] A.M. Weiner, "Femtosecond pulse shaping using spatial light modulators," Rev. Sci. Instr. **71**, 1929 (2000).

[5] J. T. Verdeyen, Laser Electronics, New Jersey: Prentice Hall, 2000, pp. 149.

[6] M. Shirasaki, IEEE Phot. Tech. Lett. **9**, 1598-1560 (1997).
[7] E. Hecht, *Optics* (Addison Wesley, Massachusetts, 1998).

[8] Ramo, Whinnery, and Van Duzer, *Fields and Waves in Communication Electronics* (John Wiley and Sons, New York, 1993).

[9] J.M. Vaughan, *The Fabry-Perot Interferometer* (Adam Hilger, Bristol, 1989).